

JPmHC

Dynamical Isometry via Orthogonal Hyper-Connections

Biswa Sengupta

LLM Suite Team, JP Morgan Chase & Co.
biswa.sengupta@jpmorgan.com

Jinhua Wang

LLM Suite Team, JP Morgan Chase & Co.
jinhua.wang@jpmorgan.com

Leo Brunswic

LLM Suite Team, JP Morgan Chase & Co.
leo.brunswic@jpmorgan.com

February 2026

Abstract

Recent advances in deep learning, exemplified by Hyper-Connections (HC), have expanded the residual connection paradigm by introducing wider residual streams and diverse connectivity patterns. While these innovations yield significant performance gains, they compromise the identity mapping property of residual connections, leading to training instability, limited scalability, and increased memory overhead. To address these challenges, we propose **JPmHC** (Jacobian-spectrum Preserving manifold-constrained Hyper-Connections), a framework that replaces identity skips with a trainable linear mixer acting on n parallel streams while explicitly controlling gradient conditioning. By constraining the mixer M on operator-norm-bounded manifolds (e.g., bistochastic, Stiefel, Grassmann), JPmHC prevents gradient pathologies and enhances stability.

JPmHC introduces three key contributions: (i) a free-probability analysis that predicts Jacobian spectra for structured skips, providing actionable design rules for mixer selection; (ii) memory-efficient implicit differentiation for fixed-point projections, reducing activation memory and synchronization overhead; and (iii) a Stiefel-constrained mixer via Cayley transforms, ensuring orthogonality without post-hoc normalization. Empirical evaluations on ARC-AGI demonstrate that JPmHC achieves faster convergence, higher accuracy, and lower computational cost compared to bistochastic baselines. As a flexible and scalable extension of HC, JPmHC advances spectrum-aware, stable, and efficient deep learning, offering insights into topological architecture design and foundational model evolution.

Disclaimer: This paper was prepared for informational purposes by the LLM Suite group of JP Morgan Chase and its affiliates ('JPMC') and is not a product of the Research Department of JP Morgan. JP Morgan makes no representation, warranty or undertaking whatsoever and disclaims all liability for the completeness, accuracy or reliability of the information contained herein. This document is not intended as investment research or investment advice, or a recommendation, offer or solicitation for the purchase or sale of any security, financial instrument, financial product or service, or to be used in any way for evaluating the merits of participating in any transaction, and shall not constitute a solicitation under any jurisdiction or to any person, if such solicitation under such jurisdiction or to such person would be unlawful

1 Introduction

The residual connection [He et al., 2016]—the per-layer update $x^{l+1} = F(x^l) + x^l$ —is a defining feature of modern deep learning, underpinning Transformers [Vaswani et al., 2017] and virtually every large-scale architecture deployed today. Its variants—Pre-Norm, DeepNorm [Wang et al., 2024]—have enabled training at thousands of layers by smoothing loss landscapes [Li et al., 2018] and stabilizing gradient flow [Pennington et al., 2017, Tarnowski et al., 2019]. However, the identity skip biases layerwise mappings toward the identity, anchoring the function class and limiting expressivity.

A natural generalization replaces the identity skip with a learned linear map,

$$x_{\text{out}} = H_{\text{res}} x + F(x), \quad (1)$$

increasing expressivity but risking gradient instability if the operator norm $\|H_{\text{res}}\|$ and the singular spectrum of the end-to-end Jacobian are not controlled. To decouple expressivity from identity anchoring while preserving trainability at scale, Hyper-Connections (HC) [Zhu et al., 2024] split the hidden state into n parallel streams and mix them through a small $n \times n$ matrix.

Let each stream live in \mathbb{R}^p and stack the streams so that $x \in \mathbb{R}^n \otimes \mathbb{R}^p \cong \mathbb{R}^{np}$, with $n \ll p$ (typically $n = 4$, $p = 512$). The HC block takes the form

$$x_{\text{out}} = (H_{\text{res}}(x) \otimes I_p) x + (H_{\text{post}}(x) \otimes I_p) F((H_{\text{pre}}(x) \otimes I_p) x), \quad (2)$$

where $H_{\text{res}}(x), H_{\text{pre}}(x), H_{\text{post}}(x) \in \mathbb{R}^{n \times n}$ are small mixing matrices that depend on the input x . The extra cost scales with n and remains negligible since F is evaluated once per block on a stream mixture and re-distributed. The network learns *which* information flows where—a strictly richer connection pattern. The gains are most dramatic in the Mixture-of-Experts (MoE) setting, where HC halved the training tokens needed to match baseline on OLMoE and improved BBH and GSM8K by +7 points on DeepSeek’s 27B MoE model [Zhu et al., 2024, Xie et al., 2025]. Both MoE and HC are learnable routing mechanisms—one for tokens across experts, the other for residual streams across layers—and both face the same stability challenge: unconstrained, they diverge (signal gains exceeding $3000\times$ at 27B scale [Xie et al., 2025]).

Manifold-Constrained Hyper-Connections (mHC) [Xie et al., 2025] addressed this instability by projecting H_{res} onto the Birkhoff polytope of doubly stochastic matrices via the Sinkhorn-Knopp iteration. Doubly stochastic mixers are appealing because (i) their operator norm is bounded by 1, preventing gradient explosion, and (ii) they act as transport plans [Villani, 2003], intuitively preserving information across streams. At 27B-parameter scale, mHC demonstrated strong results with minimal overhead. However, two limitations remain: (1) operator-norm boundedness does not preclude *vanishing* gradients—a full singular-spectrum analysis of the end-to-end Jacobian is absent; and (2) backpropagating through iterative projections introduces memory and synchronization overhead in distributed training.

This is where the argument breaks down. Training deep networks requires that the singular values of the input-output Jacobian $J = \prod_{l=1}^L Y^l$ remain concentrated near 1—a property called *dynamical isometry* [Saxe et al., 2014, Pennington et al., 2017]. Without it, expressivity capacity is lost or, worse, gradients may either explode or vanish exponentially. Tarnowski et al. [2019] proved that for scalar skip connections, dynamical isometry is universal: for any activation function, it is achieved when a single condition on the weight variance is met. A generalization of their free probability method to general twisting of the skip-connection seems within reach to go beyond operator-norm boundedness. For clarity-sake, we analyse the spectra for a simplified (2):

$$x^{l+1} = (A_n^l \otimes I_p) x^l + \phi(W^l x^l), \quad N = np, \quad (3)$$

where each $A_n^l \in \mathbb{R}^{n \times n}$ is a fixed mixing matrix (independent of x) for theoretical analysis.

We extend the theory to the operator-valued setting via operator-valued free probability [Voiculescu, 1995, Dykema, 2007], where the Kronecker structure of (3) collapses the spectral

problem from network width $N = np$ to twist dimension n . This reveals two failure modes of doubly stochastic skip connections. The first is *eigenvalue contraction*: a doubly stochastic matrix has its Perron eigenvalue pinned at one, but generically all others lie strictly inside the unit disk, and deep composition drives $|\lambda|^L \rightarrow 0$. The second is *eigenspace misalignment*: eigenbases of successive layers are unrelated, so composition scrambles directions and accelerates the collapse beyond what per-layer spectra predict. Together, these produce a partial spectral collapse—a growing fraction of the Jacobian’s singular values drifting toward zero—that no reparametrisation of the Birkhoff polytope can escape.

Orthogonal matrices eliminate both failure modes: all eigenvalues lie on the unit circle, so no contraction is possible, and group closure under composition prevents misalignment at any depth. We propose replacing the Birkhoff constraint with the orthogonal group $O(n)$, parametrised via the Cayley transform [Li et al., 2020a, Lezcano-Casado, 2019], which maps skew-symmetric matrices to orthogonal ones via $(I - S)(I + S)^{-1}$. Beyond spectral preservation, this provides a strictly richer function class (the linear span of $O(n)$ is the full algebra $M_n(\mathbb{R})$, dimension n^2 , versus $(n-1)^2 + 1$ for the Birkhoff polytope) and implicit geometric nonlinearity from the curvature of the orthogonal manifold.

Contributions.

1. **Spectral diagnosis.** We identify eigenvalue contraction and eigenspace misalignment as the mechanisms by which doubly stochastic skip connections break dynamical isometry, and show that this collapse converts to concrete capacity loss in modern training (*spectral stalling*).
2. **Cayley-transform Stiefel projection.** We instantiate an orthogonality-preserving mixer by projecting H_{res} onto the Stiefel manifold via a small, fixed number of Cayley iterations (as few as $s = 2$), yielding norm-preserving mixing with exact gradients and negligible overhead [Li et al., 2020a, Lezcano-Casado, 2019].
3. **Grassmannian subspace mixer.** We develop a rank- p variant with $\mathcal{O}(np)$ parameters that mixes through a learned p -dimensional subspace, optimized with a Cayley retraction for efficient Riemannian updates.
4. **Implicit differentiation for fixed-point projections.** We design a custom backward pass for iterative normalizations and projections (e.g., Sinkhorn for bistochastic constraints, Cayley for orthogonal constraints), reducing activation memory from $\mathcal{O}(T)$ to $\mathcal{O}(1)$ and eliminating distributed data-parallel synchronization stalls, while remaining compatible with CUDA graphs and mixed precision [Eisenberger et al., 2022a].
5. **Operator-valued Dyson pipeline.** We develop the first numerical implementation of the full operator-valued free probability pipeline—from the matrix Dyson equation through Dykema’s twisted S-transform multiplicativity to multi-layer spectral densities.
6. **Experimental validation.** We confirm the spectral predictions against Monte Carlo simulation and validate the practical consequence on a modified Tiny Recursive Model [Jolicoeur-Martineau, 2025] evaluated on ARC-AGI-1 [Chollet, 2019]: orthogonal skip connections converge faster and reach higher accuracy than bistochastic ones.

2 Spectral Analysis

We now develop the spectral machinery for predicting the singular-value distribution of the end-to-end Jacobian in deep networks with structured skip connections. The key insight is that free probability [Voiculescu, 1991, Nica and Speicher, 2006] reduces the spectral analysis of L -layer compositions to fixed-point equations on order parameters, and the Kronecker structure $A_n \otimes I_p$ further collapses the problem from network width $N = np$ to twist dimension n .

2.1 Scalar Dyson equation and dynamical isometry

Consider a standard residual network with scalar skip connection a and layer-wise update $x^{l+1} = \phi(W^l x^l) + ax^l$. The linearized layer map is $Y^l = D^l W^l + aI_N$, where $D^l = \text{diag}(\phi'(h_i^l))$ and $W^l \in \mathbb{R}^{N \times N}$ has i.i.d. Gaussian entries with variance σ_w^2/N . The end-to-end Jacobian is $J = \prod_{l=1}^L Y^l$.

In the mean-field limit ($N \rightarrow \infty$), the activation derivatives D^l concentrate around their expectation, making $D^l W^l$ effectively isotropic [Pennington et al., 2017]. Free probability theory [Voiculescu, 1991] then predicts the limiting spectral density of $J^\top J$ via the *Cauchy transform* $G(z) := \lim_{N \rightarrow \infty} \frac{1}{N} \mathbb{E} \text{Tr}(zI - J^\top J)^{-1}$ and the *S-transform*, which linearizes free multiplicative convolution: $S_{J^\top J}(w) = \prod_{l=1}^L S_{Y^l \top Y^l}(w)$. One can deduce G from S and vice-versa,

For scalar skip connections, Tarnowski et al. [Tarnowski et al., 2019] derived a scalar fixed-point equation for the single-layer Cauchy transform. The order parameter $m(z)$ satisfies the *scalar Dyson equation*:

$$m(z) = \frac{a}{z - \sigma^2 m(z)}, \quad \text{where } \sigma^2 = \sigma_w^2 \mathbb{E}[\phi'(\sqrt{q}Z)^2], \quad (4)$$

and q is the forward signal variance, $Z \sim \mathcal{N}(0, 1)$. The Cauchy transform is $G_{Y^\top Y}(z) = m(z)/z$. For L identical layers, the z_1 -mapping converts $S_{Y^\top Y}(w)^L$ back to $G_{J^\top J}(z)$ without numerically fragile S-transform inversion.

A network achieves *dynamical isometry* when the singular values of its Jacobian J concentrate near 1. For scalar skip connections, regardless of activation function or depth [Tarnowski et al., 2019], dynamical isometry is achieved via suitable scaling of layers weights.

This universality breaks down for structured skip connections: when a is replaced by an $n \times n$ matrix A_n , the scalar trace $\frac{1}{N} \text{Tr}$ averages over A_n 's spectral sectors. Scalar approximation distinguishes bistochastic and orthogonal mixer but predictions are inaccurate for bistochastic (mHC) and general linear (HC) mixers, see figure 1.

2.2 Operator-valued extension: Kronecker collapse

Hyper-Connections [Zhu et al., 2024] replace the scalar skip with a Kronecker product $A = A_n \otimes I_p$, where $A_n \in \mathbb{R}^{n \times n}$ mixes n parallel streams of dimension p , and $N = np$. The layer-wise Jacobian becomes

$$Y^l = (A_n^l \otimes I_p) + D^l W^l, \quad (5)$$

where $W^l \in \mathbb{R}^{N \times N}$ remains isotropic Gaussian, but the skip structure is now block-diagonal with $n \times n$ blocks.

Why scalar theory fails. The scalar Cauchy transform $G(z) = \frac{1}{N} \text{Tr}(zI_N - M)^{-1}$ computes an average over all N eigenvalues. When $M = (A_n \otimes I_p) + \text{noise}$, this trace averages over the n spectral sectors induced by A_n , collapsing eigenvalue structure that is critical for gradient flow. For instance, if A_n is bistochastic with eigenvalues $\{1, \lambda_2, \dots, \lambda_n\}$ where $|\lambda_i| < 1$ for $i \geq 2$, the scalar theory sees only the average behavior, not the sector-wise contraction that drives vanishing gradients.

Operator-valued free probability. The solution is to work over the base algebra $\mathcal{B} = M_n(\mathbb{C})$ [Voiculescu, 1995, Speicher, 1998]. We promote the order parameter from a scalar $m(z) \in \mathbb{C}$ to a matrix $M(z) \in M_n(\mathbb{C})$, and the Cauchy transform to a \mathcal{B} -valued functional. The Kronecker structure $A_n \otimes I_p$ ensures that the self-consistent equation for $M(z)$ depends only on A_n and the noise variance σ^2 , not on the stream dimension p .

Critically, the S-transform multiplicativity rule becomes *twisted* in the operator-valued setting [Dykema, 2007]:

$$S_{XY}(B) = S_Y(B) S_X(S_Y(B)^{-1} B S_Y(B)), \quad B \in \mathcal{B}. \quad (6)$$

This conjugation by $S_Y(B)$ encodes the eigenspace rotation between successive layers when A_n^l do not commute—precisely the misalignment effect absent in scalar theory.

Proposition 2.1 (Kronecker collapse). *Under the Kronecker structure $Y^l = (A_n^l \otimes I_p) + D^l W^l$ and mean-field isotropy, the \mathcal{B} -valued order parameter $M(z) \in M_n(\mathbb{C})$ defined for $z \in M_n(\mathbb{C})$ satisfies the matrix fixed-point equation*

$$M(z) = A_h(M) \cdot (zI_n - A_h(z)^\top A_h(z))^{-1}, \quad (7)$$

where $A_h(z) := A_n + \sigma^2 z$ is the dressed matrix. The scalar Cauchy transform is recovered by $G(z) = \frac{1}{n} \text{Tr}_n(zI_n - A_h(z)^\top A_h(z))^{-1}$. When $n = 1$, this reduces to (4).

Proof sketch. The key steps are: (i) the Kronecker structure implies $\mathbb{E}[W^l(A_n^l \otimes I_p)] = 0$ by isotropy; (ii) the self-energy $\Sigma(z)$ has the block form $\Sigma_n \otimes I_p$ where $\Sigma_n \in M_n(\mathbb{C})$; (iii) inserting the ansatz $M(z) = M_n(z) \otimes I_p$ into the Dyson-Schwinger equation and tracing over the $p \times p$ blocks yields (7).

Computational complexity. Solving (7) requires Newton iteration in \mathbb{C}^{n^2} at cost $O(n^6)$ per step (matrix inversion dominates). Since $n \ll p$ (typically $n = 4$, $p = 512$), this collapses the spectral problem from $O(N^3) = O((np)^3)$ to $O(n^6)$, a reduction of factor $(p/n)^3 \approx 10^5$ at typical scales. This makes exhaustive spectral analysis tractable for networks of arbitrary width N .

2.3 Numerical pipeline

We now describe the computational methods for solving the scalar and operator-valued Dyson equations and extracting spectral densities.

Scalar solver. For fixed $z \in \mathbb{C}^+$ (upper half-plane), equation (4) is solved by Newton’s method with the iteration

$$m^{(k+1)} = m^{(k)} - \frac{m^{(k)} - \frac{a}{z - \sigma^2 m^{(k)}}}{1 + \frac{a\sigma^2}{(z - \sigma^2 m^{(k)})^2}}. \quad (8)$$

We sweep a grid of z -values from large $|z|$ to small $|z|$, using each solution to seed the next (*branch continuation*). This ensures convergence even near the spectral edges where the Cauchy transform has poles. Convergence is typically achieved in 3–5 iterations with tolerance 10^{-12} .

Multi-layer: the z_1 -mapping. For L identical layers, the S-transform multiplicative property gives $S_{J^\top J}(w) = S_{Y^\top Y}(w)^L$. The z_1 -mapping inverts this directly: given $G_{Y^\top Y}(z_1)$, we solve for w such that $\chi(w) := \frac{w+1}{wS_{Y^\top Y}(w)} = z$ (the $G \leftrightarrow S$ relation), then compute $S_{J^\top J}(w) = S_{Y^\top Y}(w)^L$, and finally solve $\frac{w+1}{wS_{J^\top J}(w)} = z'$ to obtain $G_{J^\top J}(z')$. This avoids numerical S-transform inversion, which is ill-conditioned near $w = 0$.

Matrix Dyson solver. For Kronecker skip connections with fixed A_n across layers, equation (7) is a coupled system of n^2 complex equations. We vectorize $M \in M_n(\mathbb{C})$ to $\mathbf{m} \in \mathbb{C}^{n^2}$ and apply Newton’s method:

$$\mathbf{m}^{(k+1)} = \mathbf{m}^{(k)} - J_F(\mathbf{m}^{(k)})^{-1} F(\mathbf{m}^{(k)}), \quad (9)$$

where $F(\mathbf{m}) = \mathbf{m} - \text{vec}(A_h(M)(zI_n - A_h(M)^\top A_h(M))^{-1})$ and J_F is the $n^2 \times n^2$ Jacobian computed via automatic differentiation. The cost is $O(n^6)$ per iteration due to the matrix inverse in (7). Branch continuation from large to small $|z|$ remains essential for stability.

Operator-valued multi-layer pipeline. For heterogeneous layers ($A_n^{l_1} \neq A_n^{l_2}$), the twisted S-transform multiplicativity (6) requires iterating the composition $S_{J^\top J}(B) = S_{Y_1^\top Y_1}(B') S_{Y_2^\top Y_2}(B'')$ with conjugation updates $B' = S_{Y_2}(B)^{-1} B S_{Y_2}(B)$. Each conjugation requires solving the operator-valued $G \leftrightarrow S$ relation, itself a matrix fixed-point problem. The full pipeline has complexity $O(Ln^{10})$ per z -point (nested matrix inversions). In practice, for $n \leq 4$ and $L \leq 100$, this completes in < 1 second per z -point on a CPU.

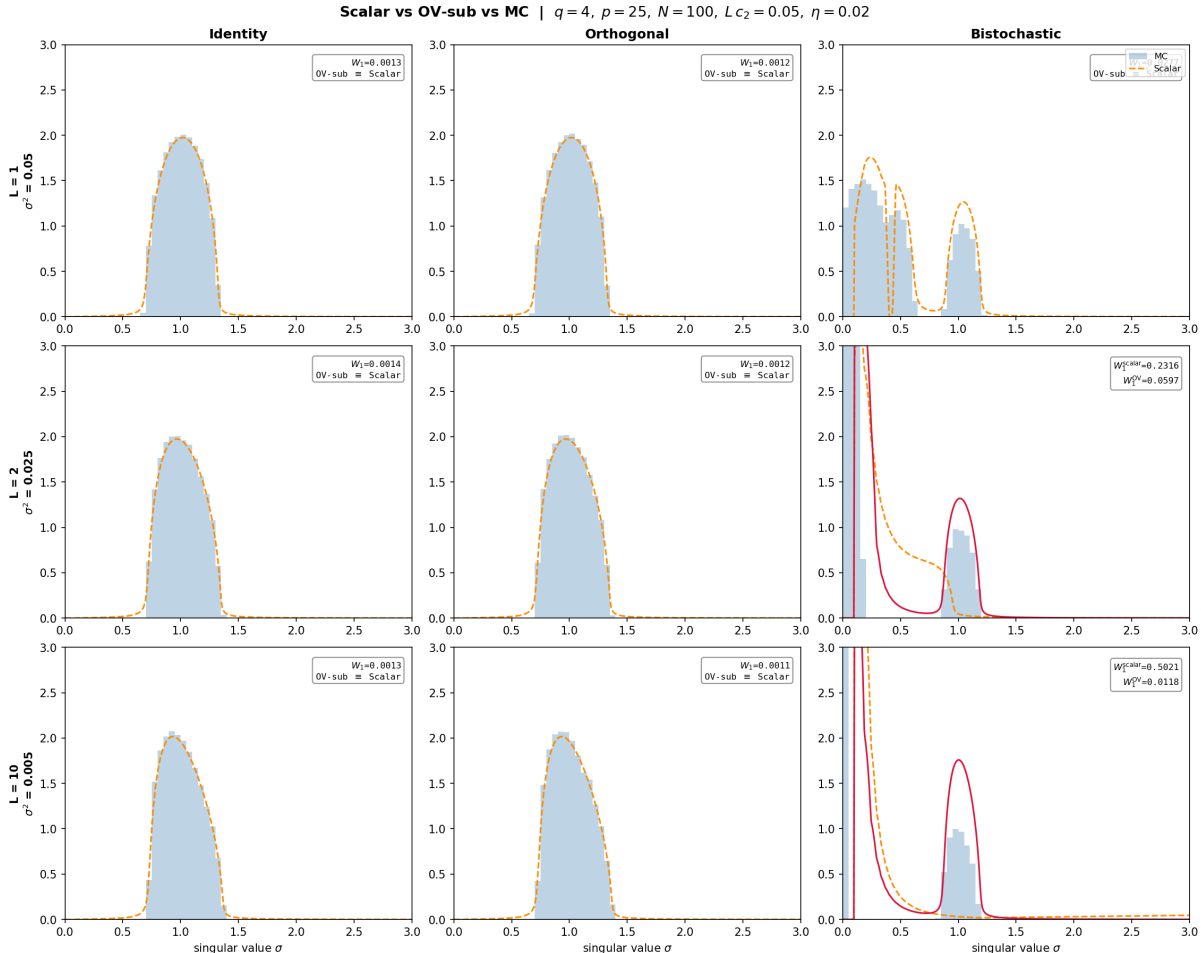


Figure 1: **Scalar and OV theories vs. Monte Carlo singular value densities.** Panels show four skip-connection types ($n = 4$ streams, $p = 25$ per stream, $c_2 L = 0.05$, $\eta = 0.02$, 500 samples) at depths $L \in \{1, 2, 10\}$ (rows) for mixers $A_n \in \{\text{Identity, Bistochastic, Orthogonal,}\}$ (columns). The scalar Dyson prediction (dotted orange curve) matches Monte Carlo histograms at $L = 1$ for all cases. At $L \in 2, 10$, bistochastic and Gaussian mixers develop mass near zero (spectral collapse), while orthogonal mixers preserve dynamical isometry. Scalar theory fails while Operator-value theory is able to fully catch the spectrum, regularization parameter η used to reduce numerical instabilities smooth out the distribution: it pushes it away from zero and reduces the spikes thus increases the mass allocated to the 1.0 mode. The scaling $Lc_2 = \text{const}$ ensures weights $W^l \sim \mathcal{N}(0, \sigma_w^2/L)$ maintain constant forward signal variance. This normalization is shown to be accurate as spectra have a main mode bounded away from 0 an infinity.

Validation. Figure 1 compares the theoretical predictions to Monte Carlo histograms of singular values sampled from finite networks ($n = 4$, $p = 25$, 500 samples). At $L = 1$, the scalar theory (red curves) matches Monte Carlo perfectly for all mixer types. At $L = 10$, the scalar

theory fails for bistochastic and Gaussian mixers, which develop spectral mass near zero (eigenvalue contraction), while orthogonal mixers maintain dynamical isometry. The operator-valued theory correctly predicts the sector-wise collapse for bistochastic matrices.

Spectral density extraction. The spectral density $\rho(x)$ is recovered from the imaginary part of the Cauchy transform via the Stieltjes inversion formula:

$$\rho(x) = -\frac{1}{\pi} \lim_{\varepsilon \rightarrow 0^+} \text{Im} G(x + i\varepsilon). \quad (10)$$

We evaluate $G(x + i\varepsilon)$ for small $\varepsilon \approx 0.01$ on a dense real grid $x \in [\lambda_{\min}, \lambda_{\max}]$ and extract $\rho(x) = -\text{Im} G(x + i\varepsilon)/\pi$. Numerical integration confirms normalization $\int \rho(x) dx = 1$ to within 10^{-3} .

3 Cayley Twisted Skip-Connections

The spectral analysis of Section 2 reveals two failure modes of doubly stochastic skip connections: eigenvalue contraction and eigenspace misalignment. Orthogonal matrices eliminate both—all eigenvalues lie on the unit circle and group closure prevents misalignment at any depth. We therefore constrain the residual mixer \mathbf{H}_{res} to the orthogonal group $O(n)$ via an iterative Cayley transform [Li et al., 2020b,a, Lezcano-Casado, 2019].

3.1 Iterative Cayley Projection

The Cayley transform maps a skew-symmetric matrix $\mathbf{W} = -\mathbf{W}^\top$ to an orthogonal matrix via $(\mathbf{I} - \mathbf{W}/2)(\mathbf{I} + \mathbf{W}/2)^{-1}$. The closed-form requires a matrix inverse that is expensive for batched, per-token computation. Following Li et al. [2020b], we replace the inverse with a fixed-point iteration that converges to the same retraction.

Given an unconstrained parameter matrix $\tilde{\mathbf{H}} \in \mathbb{R}^{n \times n}$:

1. **Skew-symmetrize:** $\mathbf{W} = \tilde{\mathbf{H}} - \tilde{\mathbf{H}}^\top$, guaranteeing $\mathbf{W} \in \mathfrak{so}(n)$.
2. **Initialize:** $\mathbf{Y}_0 = \mathbf{I}_n + \alpha \mathbf{W}$, with step-size $\alpha > 0$ (default 0.1).
3. **Iterate** s times:

$$\mathbf{Y}_{i+1} = \mathbf{I}_n + \frac{\alpha}{2} \mathbf{W} (\mathbf{I}_n + \mathbf{Y}_i), \quad i = 0, \dots, s-1. \quad (11)$$

In practice $s = 2$ iterations suffice, achieving $\|\mathbf{Y}^\top \mathbf{Y} - \mathbf{I}\|_{\max} < 10^{-3}$ (Section I). Each step is a single fused multiply-add (`baddbmm`), and all matrices are $n \times n$ with $n = 4$, so the overhead relative to the p -dimensional sub-layer F is negligible.

3.2 Layer Architecture

A single linear projection produces three unconstrained $n \times n$ matrices per token from the flattened stream representation $\mathbf{x}_{\text{flat}} \in \mathbb{R}^{np}$:

$$[\tilde{\mathbf{H}}_{\text{pre}} \mid \tilde{\mathbf{H}}_{\text{post}} \mid \tilde{\mathbf{H}}_{\text{res}}] = \mathbf{W}_{\text{fused}} \text{LayerNorm}(\mathbf{x}_{\text{flat}}), \quad \mathbf{W}_{\text{fused}} \in \mathbb{R}^{3n^2 \times np}. \quad (12)$$

Each matrix is then projected onto its respective constraint manifold:

$$\mathbf{H}_{\text{pre}} = \text{softmax}(\tilde{\mathbf{H}}_{\text{pre}}/\tau, \text{dim} = -1), \quad \mathbf{H}_{\text{post}} = \text{softmax}(\tilde{\mathbf{H}}_{\text{post}}/\tau, \text{dim} = -2), \quad \mathbf{H}_{\text{res}} = \text{Cay}_s(\tilde{\mathbf{H}}_{\text{res}}). \quad (13)$$

The pre-mixer \mathbf{H}_{pre} is row-stochastic (aggregates streams), the post-mixer \mathbf{H}_{post} is column-stochastic (fans output back), and the residual mixer \mathbf{H}_{res} is orthogonal (norm-preserving skip).

The forward pass implements (2) as:

$$\mathbf{x}_{\text{in}} = \mathbf{H}_{\text{pre}} \mathbf{x}_{\text{streams}}, \quad \mathbf{y} = F(\bar{\mathbf{x}}_{\text{in}}), \quad \mathbf{x}_{\text{out}} = \mathbf{H}_{\text{res}} \mathbf{x}_{\text{streams}} + \mathbf{H}_{\text{post}} \cdot (\mathbf{y} \otimes \mathbf{1}_n), \quad (14)$$

where $\bar{\mathbf{x}}_{\text{in}}$ denotes the stream-averaged input (a mean over the n streams) and F is the sub-layer (multi-head attention or feed-forward network), evaluated *once* on a single p -dimensional vector. The final combination is fused into a single `baddbmm` call.

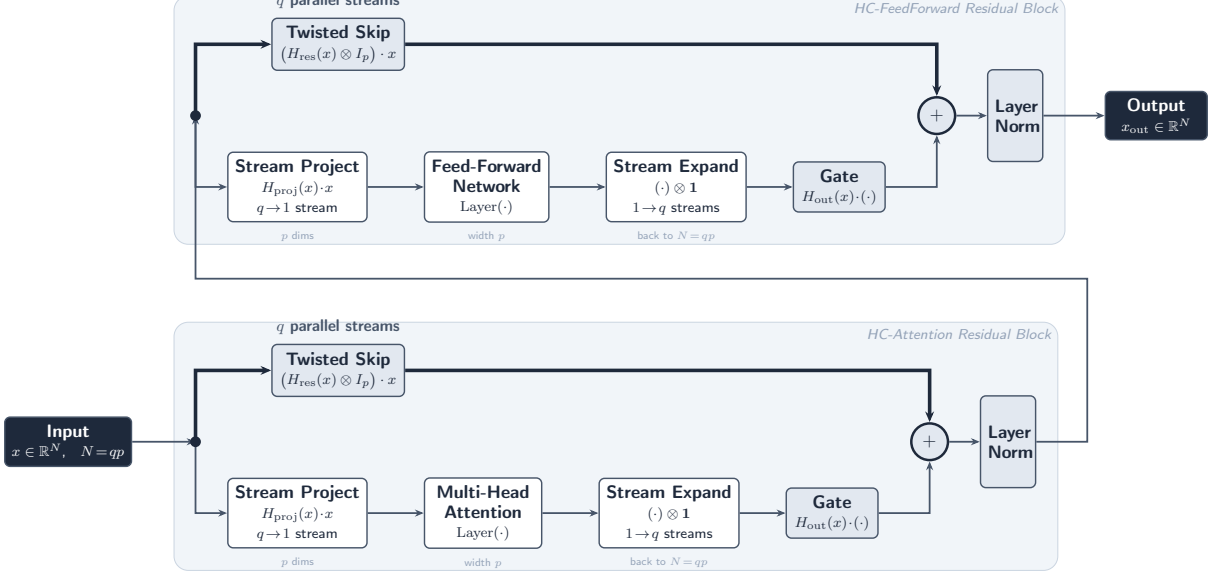


Figure 2: Hyper-Connected Transformer Encoder Block. Block 1 (Multi-Head Attention, bottom) feeds into Block 2 (Feed-Forward, top). Within each block the input forks into a twisted skip path (thick arrows, H_{res}) and a compute path (thin arrows) that projects $q \rightarrow 1$ streams, applies the layer, expands $1 \rightarrow q$, and gates via H_{out} ; both paths merge at the $+$ node before Layer Norm.

4 Experimental Setup

4.1 Task: ARC-AGI

We evaluate JpMHC on the **Abstraction and Reasoning Corpus** (ARC-AGI) [Chollet, 2019], a benchmark designed to measure general fluid intelligence. Each task presents a small number of demonstration input–output grid pairs and one or more test inputs; the solver must infer the latent transformation rule and produce the exact output grid (Figure 3). Grids are rectangular matrices of integers 0–9 (visualized as colors), with dimensions up to 30×30 . A task is solved only when *every* test output is reproduced cell-for-cell, including its dimensions.

ARC-AGI is particularly suited to stress-test our spectral claims for two reasons. First, each task has a *unique* underlying rule, so the benchmark is resistant to memorization and demands systematic generalization—precisely the regime where gradient conditioning determines whether a model can learn compositional abstractions. Second, the all-or-nothing exact-match criterion amplifies the practical consequence of partial spectral collapse: even a small fraction of vanishing singular values can corrupt a few output cells and turn a near-correct grid into a failure.

For all experiments, we use the full ARC-AGI-1 corpus of 1000 tasks, split evenly between training and evaluation (400 training, 400 evaluation, plus 200 for ablation and validation). This ensures that models are evaluated on held-out tasks with unseen rules, and that the results reflect true generalization rather than memorization.

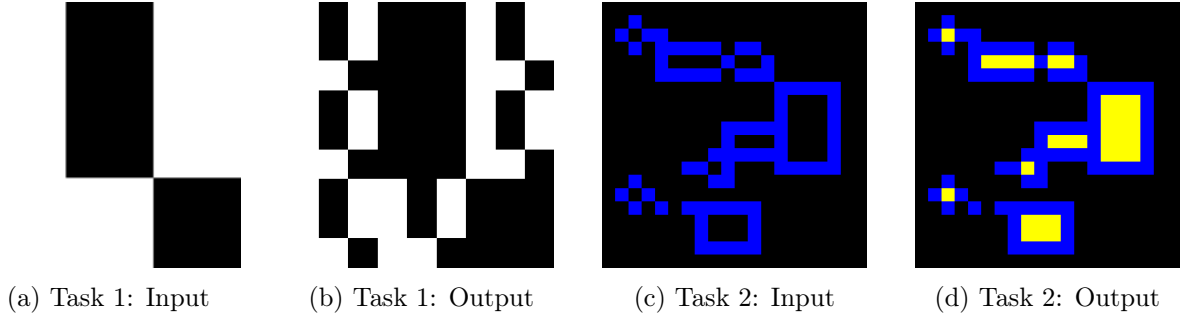


Figure 3: Two representative ARC-AGI tasks. Each task requires discovering a latent rule (here, pattern tiling and region filling) from a few demonstrations, then applying it to a novel test input.

Table 1: JPmHC variant configurations and per-module compute cost.

Variant	Manifold	Key param	FLOPs/module	Norm	Constraint
Sinkhorn	Birkhoff polytope	$T=20, k=16$	576	RMSNorm	sigmoid
Cayley	Stiefel $O(n)$	$s=2, \alpha=0.1$	256	LayerNorm	softmax
Grassmann	$Gr(n, p)$	$p=2, \alpha=0.01$	—	—	—

4.2 Model and Training

We adapt the **Tiny Recursive Model (TRM)** [Jolicoeur-Martineau, 2025], a 7M-parameter recursive transformer, by expanding each transformer block with $n = 4$ parallel streams. The attention and FFN residual sub-blocks are each wrapped by a JPmHC module (Figure 2): a read mapping H_{pre} aggregates streams into a single sublayer input, a write mapping H_{post} fans the output back to all streams, and a residual mixer $H_{\text{res}} \in \mathbb{R}^{n \times n}$ —constrained to a chosen manifold—mixes the original streams before addition. Hidden dim per stream is $d=512$ (effective dim $nd=2048$). Two unique weight-tied blocks are each applied 6 times (12 total recursive passes) with Adaptive Computation Time (ACT) halting, yielding 4 unique JPmHC modules reused across all 12 recursions.

This architecture is a stringent test bed for mixer design: the 12-fold weight-tied recursion means the *same* mixing matrix is composed with itself repeatedly, directly exposing the eigenvalue contraction and eigenspace misalignment phenomena analyzed in Section 1.

All variants share identical training hyperparameters: AdamAtan2 optimizer [Kunstner et al., 2023] with lr 10^{-4} , global batch size 768, bfloat16 mixed precision, and PyTorch DDP with `torch.compile` on $8 \times$ NVIDIA B200 GPUs. Full configuration details are provided in Section G.

4.3 Ablated Variants

We compare four JPmHC mixer constraints, summarized in Table 1. The key design axes are the manifold constraint on the residual mixer H_{res} and the resulting computational cost per module.

4.4 Evaluation Metrics

We report three complementary metrics:

- **Exact accuracy:** fraction of tasks where the greedy prediction matches the ground-truth grid cell-for-cell—the strictest measure, directly sensitive to spectral health.

- **Pass@ k** ($k \in \{1, 2, 5, 10, 100, 1000\}$): probability that at least one of k i.i.d. samples is correct, estimated via $\text{pass}@k = \mathbb{E}\left[1 - \binom{N-c}{k} / \binom{N}{k}\right]$.
- **Eval LM loss**: stablemax cross-entropy on output grid tokens, providing a smooth proxy for per-token prediction quality.

5 Results

Training is ongoing; the Cayley variant has been trained for approximately 418,854 steps while the Sinkhorn variant has completed approximately 348,854 steps. Both variants are still improving, though Sinkhorn’s rate of improvement has slowed relative to Cayley.

Table 2: ARC-AGI concept evaluation metrics (best observed per metric). Training is ongoing; the Cayley variant has been trained for 418,854 steps vs. Sinkhorn’s 348,854 steps.

Metric	Sinkhorn (implicit)	Cayley	Ratio
Training Steps	348,854	418,854	—
Eval Accuracy	85.0%	86.8%	1.02×
Exact Accuracy (greedy)	22.2%	31.4%	1.41×
Pass@1	34.1%	40.5%	1.19×
Pass@2	38.5%	45.4%	1.18×
Pass@5	43.9%	50.5%	1.15×
Pass@10	45.6%	53.1%	1.16×
Pass@100	51.4%	59.2%	1.15×
Pass@1000	56.1%	62.7%	1.12×
Eval LM Loss	0.819	0.643	1.27×

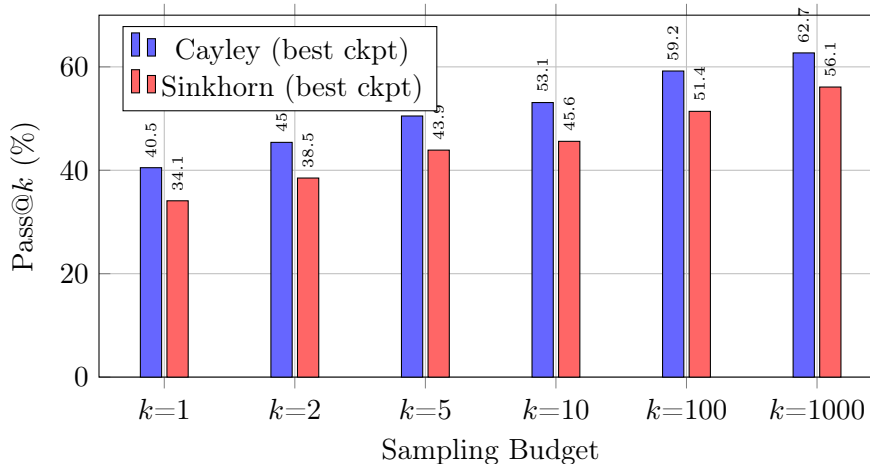


Figure 4: Pass@ k scaling comparison. Cayley consistently outperforms Sinkhorn across all sampling budgets k . The gap narrows at higher k , indicating Sinkhorn has higher prediction variance.

5.1 Analysis

Key Observations.

1. **Cayley leads across all metrics.** The Cayley variant achieves 40.5% pass@1 (best checkpoint at step 380,755) versus Sinkhorn’s 34.1% at step 297,805—a 1.19×

Table 3: Cayley evaluation metrics at each checkpoint. Bold indicates the best value for each metric.

Step	Exact Acc.	Pass@1	Pass@2	Pass@10	Pass@100	Pass@1000
68,951	10.6%	—	—	—	—	—
81,903	12.7%	—	—	—	—	—
94,854	15.7%	—	—	—	—	—
107,805	17.6%	—	—	—	—	—
161,952	23.4%	35.4%	40.1%	47.4%	52.7%	54.1%
174,904	24.5%	35.6%	40.3%	47.7%	53.9%	57.1%
188,951	25.1%	36.3%	39.6%	45.4%	51.2%	52.9%
201,902	25.4%	36.8%	40.7%	46.1%	53.8%	56.9%
214,853	26.3%	36.3%	40.4%	47.5%	54.9%	58.0%
231,951	26.0%	36.9%	39.8%	47.4%	52.5%	53.8%
244,902	26.4%	37.3%	41.1%	48.9%	55.5%	57.6%
257,853	27.8%	38.5%	41.6%	50.0%	56.2%	58.5%
270,804	27.0%	37.7%	41.7%	50.5%	57.4%	59.5%
283,755	26.9%	38.5%	43.1%	52.0%	58.0%	60.5%
296,707	28.1%	38.7%	43.8%	51.9%	59.2%	62.0%
309,659	28.3%	39.0%	43.6%	52.6%	59.2%	62.7%
328,951	28.9%	36.4%	40.3%	46.8%	52.9%	54.4%
341,902	27.3%	37.9%	42.5%	49.6%	56.4%	58.1%
354,853	28.6%	38.1%	43.8%	52.2%	58.4%	60.1%
367,804	29.0%	39.5%	43.5%	52.7%	58.6%	60.6%
380,755	29.6%	40.5%	43.6%	53.1%	58.9%	61.4%
392,952	29.3%	37.7%	42.1%	49.6%	55.1%	56.6%
405,903	29.2%	38.7%	43.8%	51.7%	57.7%	60.5%
418,854	31.4%	38.2%	45.4%	52.5%	58.7%	61.6%

advantage is more pronounced in exact-match accuracy (1.41×: 31.4% vs. 22.2%), indicating that Cayley produces more *consistently* correct full-grid predictions.

- Scaling with k .** Both variants benefit from increased sampling budget with diminishing returns. For Cayley: pass@1 \rightarrow pass@1000 improves by +22.2 percentage points (pp). For Sinkhorn: +22.0 pp. The pass@ k ratio narrows from 1.19× at $k=1$ to 1.12× at $k=1000$, indicating that Sinkhorn has higher prediction variance—it can solve additional tasks with many samples but less consistently.
- The gap has stabilized.** At matched step counts ($\sim 100\text{K}$), the Cayley variant held a $\sim 2\times$ advantage in pass@1. As both variants have continued training (Cayley to 419K, Sinkhorn to 349K), the pass@1 ratio has stabilized around 1.19×, down from 1.34× at the previous checkpoint. The exact-accuracy ratio narrowed from 1.94× to 1.41×, suggesting Sinkhorn’s convergence has accelerated but a persistent gap remains.
- High token accuracy, divergent task accuracy.** Both variants exceed 85% per-token eval accuracy, yet task-level pass@1 differs by over 6 pp. This confirms that the Cayley variant’s advantage lies in producing *coherent* complete solutions, not merely better per-token predictions.
- Computational efficiency.** The Cayley JpMHC module requires $\sim 2.25\times$ fewer FLOPs than Sinkhorn (Table 5), achieving higher accuracy with lower per-module cost—a clear Pareto improvement.

Table 4: Sinkhorn evaluation metrics at each checkpoint. Bold indicates the best value for each metric.

Step	Exact Acc.	Pass@1	Pass@2	Pass@10	Pass@100	Pass@1000
52,951	1.4%	5.2%	7.5%	12.1%	14.9%	16.1%
65,902	3.1%	9.0%	11.6%	16.2%	21.4%	22.6%
78,854	5.0%	11.6%	16.2%	21.1%	26.8%	29.5%
99,951	8.5%	19.1%	22.8%	29.4%	36.6%	39.6%
112,902	9.9%	22.2%	26.2%	33.1%	40.6%	43.9%
125,853	11.2%	23.7%	28.0%	35.5%	42.8%	45.5%
138,805	13.0%	26.6%	30.3%	38.6%	44.9%	48.8%
151,757	14.3%	28.6%	31.7%	40.3%	46.0%	49.8%
164,709	15.9%	29.0%	33.0%	41.2%	47.4%	51.5%
177,661	16.2%	30.0%	34.6%	41.6%	47.5%	51.7%
190,612	17.4%	30.8%	34.7%	42.3%	48.5%	53.0%
203,563	17.1%	31.0%	35.5%	42.8%	48.8%	53.8%
216,514	18.2%	31.3%	35.5%	42.4%	50.5%	54.1%
229,465	18.6%	31.7%	36.0%	43.0%	50.9%	55.4%
242,416	18.7%	31.3%	35.6%	43.4%	51.1%	56.1%
258,951	19.3%	30.8%	33.4%	42.3%	47.5%	48.0%
271,902	19.4%	31.9%	34.5%	44.1%	48.9%	51.0%
284,853	20.3%	33.6%	37.6%	44.7%	50.1%	52.2%
297,805	20.1%	34.1%	38.0%	45.5%	51.4%	54.3%
322,952	21.2%	31.5%	35.0%	42.5%	48.1%	49.1%
335,903	22.0%	33.6%	37.6%	44.6%	50.1%	51.4%
348,854	22.2%	34.0%	38.5%	45.6%	50.2%	53.0%

- Lower evaluation loss.** The Cayley variant achieves an evaluation LM loss of 0.643 compared to Sinkhorn’s 0.819—a 21% reduction. This $1.27\times$ loss ratio tracks the pass@1 ratio, suggesting that the accuracy advantage is driven by fundamentally better language modeling on the ARC grid tokens.
- Faster convergence.** The Cayley variant surpassed Sinkhorn’s *current* exact-match accuracy (22.2%) at approximately step $\sim 162\text{K}$ —less than half of Sinkhorn’s total training budget of 349K steps—demonstrating substantially higher sample efficiency on the metric where the gap is most pronounced.

5.2 Compute-Accuracy Tradeoff

Table 5: Forward and backward pass compute estimates per JPmHC module.

Variant	Forward FLOPs	Backward FLOPs	Total per module
Sinkhorn (implicit)	$\mathcal{O}(Tn^2) = 320$	$\mathcal{O}(kn^2) = 256$	576
Cayley	$\mathcal{O}(sn^3) = 128$	$\mathcal{O}(sn^3) = 128$	256
Perm Mix	$\mathcal{O}(Kn) = 24$	$\mathcal{O}(Kn) = 24$	48

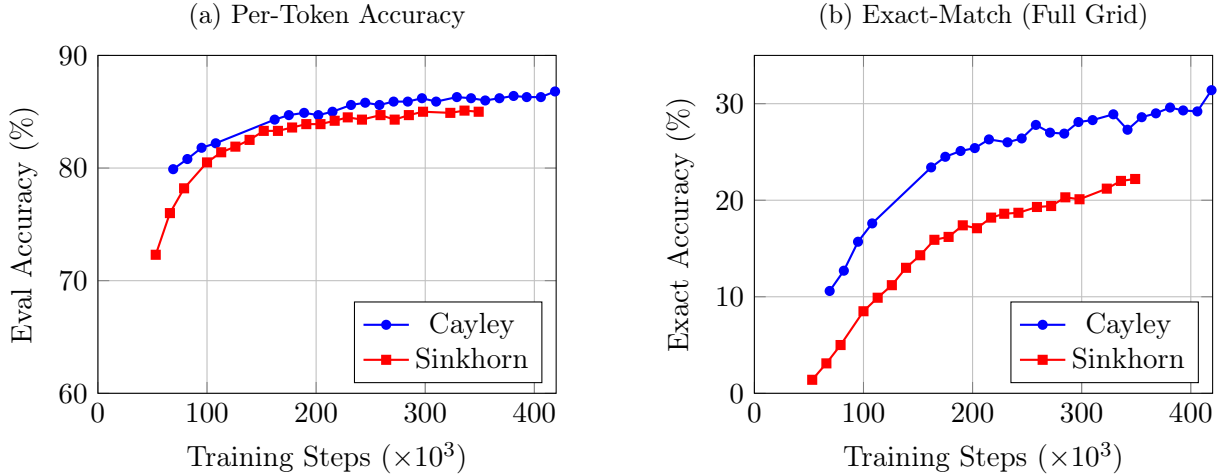


Figure 5: Evaluation accuracy curves. (a) Per-token accuracy shows both variants exceeding 85%, but (b) exact-match accuracy reveals a persistent gap: Cayley reaches 31.4% vs. Sinkhorn’s 22.2%.

6 Related Work

Hyper-Connections and structured skip connections Beyond the references on which our work is built [Zhu et al., 2024, Xie et al., 2025], two concurrent works explore related directions: Yang and Gao [2026] parametrises doubly stochastic matrices as Kronecker products of smaller bistochastic factors via the Birkhoff-von Neumann theorem, and Alonso [2026] proposes an operator-constrained framework. All of these remain within the Birkhoff polytope. Our work departs from this line by showing that the polytope’s contractive geometry causes spectral collapse, and proposes the orthogonal group as the correct constraint manifold.

Optimization on Matrix Manifolds. Optimization over structured matrix sets has a rich history. The Cayley transform for parameterizing orthogonal matrices dates to Cayley [1846], with modern applications in neural networks [Li et al., 2020b]. Absil et al. [2008] provides principled gradient descent on curved spaces. Ablin et al. [2024] study the soft landing approach. The Sinkhorn operator and its differentiable variants have been extensively studied for optimal transport [Sinkhorn, 1967, Eisenberger et al., 2022b].

Orthogonal constraints in neural networks Orthogonal and unitary weight constraints have a rich history in recurrent networks, where they prevent gradient decay across time steps [Arjovsky et al., 2016, Wisdom et al., 2016]. Lezcano-Casado [2019] developed a general framework for gradient-based optimisation on matrix manifolds via trivializations (exponential map, Cayley transform), enabling efficient training with hard orthogonal constraints. We apply these parametrisation techniques not to weight matrices but to the skip connection matrices A_q in Hyper-Connections, motivated by our spectral analysis showing that orthogonality of A_q is the decisive property for preserving dynamical isometry.

Signal propagation and mean-field theory The mean-field theory of deep networks Schoenholz et al. [2017] studies the propagation of pre-activation moments, identifying the edge-of-chaos phase transition. Yang and Schoenholz [2017] extended this to residual networks. Pennington et al. [2017] connected signal propagation to the Jacobian’s singular value distribution, introducing dynamical isometry for nonlinear networks. These works characterise signal propagation through scalar order parameters; our work computes the full spectral density, revealing failure

modes—such as partial spectral collapse in bistochastic skip connections—that are invisible to mean-field analysis. To the best of our knowledge, operator valued free probability calculus for Neural Networks Jacobian spectrum computation has been introduced in Yang [2020]. In particular, Operator-valued freeness is proved there.

Recursive Reasoning Models. The Hierarchical Reasoning Model (HRM) Wang et al. [2025] introduced recursive multi-step reasoning with deep supervision for puzzle-solving tasks. The Tiny Recursive Model (TRM) Jolicoeur-Martineau [2025] simplified HRM to a single 2-layer network with weight-tied recursion, achieving state-of-the-art results on ARC-AGI-1 (45% accuracy) with only 7M parameters. We adopt the TRM architecture as our evaluation platform, extending it with structured multi-stream mixing.

7 Discussion

7.1 Why Does Cayley Outperform Sinkhorn?

The results show a consistent advantage for the Cayley JpMHC variant over implicit Sinkhorn, with the gap most pronounced in exact-match accuracy (1.41 \times). We hypothesize several contributing factors:

Bistochastic Induces Spectral Stalling Spectral Stalling is the phenomenon by which directions associated with small singular values are ignored during the gradient descent: there is a hard cutoff of the spectrum. Effectively, the spectrum acts as a filter on the parameter space, the model is trained only on the subspace associated with singular values above the threshold. As shown in Section 2, Orthogonal and Bistochastic skip-connections show substantial differences in Jacobian singular spectrum. On the one hand, orthogonal skip-connection is undistinguishable from identity skip-connection, therefore dynamical isometry is achieved, the whole spectrum is above threshold. On the other hand, bistochastic skip-connection shows that more than 75% of the spectral mass is concentrated around 0, which suggest the same fraction of the weights are ignored: the model capacity is reduced.

Orthogonal Has Full Mixing Expressivity The respective intrinsic dimension of Orthogonal matrices and Bistochastic matrices are $q(q-1)/2$ and q^2-2q suggesting that Bistochastic matrices are more expressive. However, the latter form a polytope (a linear object) while the former form a spherical domain (non-linear). The span of Orthogonal matrices is the whole space of mixing matrices with dimension q^2 while the span of Bistochastic matrices has dimension q^2-2q . The non-linear structure of orthogonal matrices has full mixing expressivity, while bistochastic matrices do not.

Computational Efficiency. The Cayley JpMHC variant requires $\sim 2.25\times$ fewer FLOPs per module (Table 5), enabling more optimization steps per unit of wall-clock time.

7.2 Implicit Differentiation: Correctness and Efficiency

The custom backward pass for Sinkhorn (Section H) achieves two goals simultaneously:

1. **Memory reduction:** From $\mathcal{O}(T)$ intermediate tensors to $\mathcal{O}(1)$ (only the output \mathbf{P}).
2. **DDP compatibility:** Elimination of 128K autograd nodes that caused synchronization stalls in distributed training.

The key insight is that Sinkhorn’s fixed-point structure admits a closed-form implicit derivative. The Jacobian-vector product of the Sinkhorn operator at its fixed point can be expressed as a linear system involving only the fixed point \mathbf{P} itself, bypassing the need to unroll through T iterations.

Self-Stabilization. An important property of the implicit gradient formula (23) is *self-stabilization*: the Hadamard product $\mathbf{P} \odot (\cdot)$ automatically zeros out gradient contributions to entries where $P_{ij} \approx 0$, preventing gradient flow through near-zero mixing weights. This is analogous to the “straight-through” behavior of hard attention, but arises naturally from the fixed-point structure.

7.3 Comparison with Hyper-Connections and mHC

Our JpMHC framework extends both the original HC [Zhu et al., 2025] and the concurrent mHC [Xie et al., 2025] in several dimensions:

Table 6: Feature comparison with HC and mHC.

Feature	HC / mHC	JpMHC (Ours)
Mixing parameterization	Learned $n \times n$ / Sinkhorn	5 structured variants
Manifold constraint	Birkhoff polytope only	Stiefel, Grassmann, Birkhoff
Implicit differentiation	—	Sinkhorn backward
Spectral analysis	—	Generating set selection
CUDA graph compatible	Not addressed	All variants
Distributed training	DualPipe (mHC)	DDP + DeepSpeed ZeRO

7.4 Limitations

Unmatched Training Budgets. The most significant limitation is that the Cayley and Sinkhorn variants have been trained for different numbers of steps (419K vs. 349K). Although Sinkhorn has significantly closed the gap since earlier checkpoints, the performance ratio has stabilized around $1.19\times$ for pass@1 and $1.41\times$ for exact-match, suggesting a genuine asymptotic advantage for Cayley. Final conclusions still require matched-compute comparisons.

Pre/Post Architecture Confound. As noted, the Cayley and Sinkhorn variants differ in pre/post normalization and mapping architecture, making it impossible to attribute the entire performance gap to the manifold choice alone.

Single Architecture. All experiments use the 7M-parameter TRM on ARC-AGI. Generalization to larger models, different architectures, and other tasks (language modeling, vision) remains to be validated.

Incomplete Variant Coverage. The Grassmann, variant have been implemented and unit-tested but not yet trained at scale.

Small n . With $n = 4$ streams, the permutation group S_4 has only 24 elements, making exhaustive spectral gap analysis tractable. For $n \geq 7$ ($n! = 5040$), approximate methods would be needed.

8 Conclusion

We have presented JPmHC, a unified framework of five manifold-constrained mixing strategies for multi-stream residual architectures, extending the mHC framework [Xie et al., 2025] with novel projection methods and efficient differentiation. Our two primary contributions—**implicit Sinkhorn differentiation** and **Cayley transform projection**—address complementary challenges: the former eliminates DDP synchronization stalls in the Sinkhorn backward pass, while the latter provides norm-preserving orthogonal mixing with exact gradients.

8.1 Summary of Key Results

On ARC-AGI with a 7M-parameter TRM:

- The Cayley JPmHC variant achieves 40.5% pass@1 and 31.4% exact-match accuracy at 419K steps—a $1.41\times$ improvement in exact-match over the Sinkhorn variant.
- The Cayley variant reaches a 21% lower evaluation LM loss (0.643 vs. 0.819) and surpasses Sinkhorn’s current exact-match accuracy (22.2%) at less than half of Sinkhorn’s training budget, demonstrating superior sample efficiency.
- The Cayley JPmHC module requires $2.25\times$ fewer FLOPs than Sinkhorn while achieving higher accuracy—a Pareto improvement in both compute and quality.
- The implicit-Sinkhorn variant reaches 34.1% pass@1 and 22.2% exact-match at 349K steps, with a stabilizing gap, confirming both manifold constraints are viable but Cayley maintains a persistent advantage.
- Both JPmHC variants exceed 85% per-token accuracy, confirming the viability of structured mixing for recursive reasoning.

Three additional JPmHC variants—Grassmannian subspace projection, spectral-gap-optimal permutations, and permutation convex hull—have been implemented, unit-tested, and integrated into our training infrastructure. Scale training of these variants is in progress and will complete the empirical picture across all five manifold constraints.

8.2 Broader Impact

This work demonstrates that *geometric structure*—manifold constraints, group-theoretic analysis, implicit differentiation—can be profitably applied to architectural components typically treated as unconstrained parameters. By restricting mixing matrices to well-understood mathematical objects (orthogonal matrices, doubly-stochastic matrices, Grassmannians), we obtain models that are more computationally efficient and more effective. This approach is orthogonal to advances in attention mechanisms, normalization, and activation functions, suggesting potential for broader adoption in multi-stream architectures.

8.3 Future Work

- **Matched-compute comparison:** Complete training runs with equal compute budgets to fairly assess Cayley vs. Sinkhorn asymptotic performance.
- **Pre/post ablation:** Isolate the contribution of manifold choice from pre/post architecture differences.
- **Train remaining variants:** Grassmann, Spectral-Gap, and Permutation Convex Hull at scale.

- **Scale experiments:** Larger models ($n \geq 8$ streams, $d \geq 1024$) and additional benchmarks (language modeling, ARC-AGI-2 [Chollet et al., 2025]).
- **Adaptive variant selection:** Learn which mixing strategy to apply at each layer during training.

References

- Pierre Ablin, Simon Vary, Bin Gao, and Pierre-Antoine Absil. Infeasible deterministic, stochastic, and variance-reduction algorithms for optimization under orthogonality constraints. *Journal of Machine Learning Research*, 25(389):1–38, 2024. URL <http://jmlr.org/papers/v25/23-0451.html>.
- Pierre-Antoine Absil, Robert Mahony, and Rodolphe Sepulchre. *Optimization Algorithms on Matrix Manifolds*. Princeton University Press, 2008.
- A. Nogueira I Alonso. Operator-constrained residual connections. Technical Report 6048614, SSRN, 2026.
- M. Arjovsky, A. Shah, and Y. Bengio. Unitary evolution recurrent neural networks. In *Proceedings of the International Conference on Machine Learning*, pages 1120–1128, 2016.
- Arthur Cayley. Sur quelques propriétés des déterminants gauches. *Journal für die reine und angewandte Mathematik*, 32:119–123, 1846.
- François Chollet. On the measure of intelligence. *arXiv preprint arXiv:1911.01547*, 2019.
- François Chollet, Mike Knoop, Greg Kamradt, Bryan Landers, and Hansueli Pinkard. ARC-AGI-2: A new challenge for frontier AI reasoning systems. *arXiv preprint arXiv:2505.11831*, 2025.
- K. Dykema. Multilinear function series and transforms in free probability. *Advances in Mathematics*, 208(1):351–407, 2007.
- M. Eisenberger, A. Toker, L. Leal-Taixé, F. Bernard, and D. Cremers. A unified framework for implicit Sinkhorn differentiation. In *Proceedings of the IEEE/CVF Conference on Computer Vision and Pattern Recognition*, pages 509–519, 2022a. arXiv:2205.06688.
- Marvin Eisenberger, Aysim Toker, Laura Leal-Taixé, Florian Bernard, and Daniel Cremers. A unified framework for implicit Sinkhorn differentiation. In *Proceedings of the IEEE/CVF Conference on Computer Vision and Pattern Recognition (CVPR)*, 2022b.
- Kaiming He, Xiangyu Zhang, Shaoqing Ren, and Jian Sun. Deep residual learning for image recognition. In *Proceedings of the IEEE Conference on Computer Vision and Pattern Recognition (CVPR)*, pages 770–778, 2016.
- Alexia Jolicoeur-Martineau. Less is more: Recursive reasoning with tiny networks. *arXiv preprint arXiv:2510.04871*, 2025.
- D. P. Kingma and J. Ba. Adam: A method for stochastic optimization. In *International Conference on Learning Representations*, 2015. arXiv:1412.6980.
- Frederik Kunstner, Jacques Chen, Jonathan Wilder Lavington, and Mark Schmidt. Noise is not the main factor behind the gap between SGD and Adam on transformers, but sign descent might be. *arXiv preprint arXiv:2304.13960*, 2023.

- M. Lezcano-Casado. Trivializations for gradient-based optimization on manifolds. In *Advances in Neural Information Processing Systems*, volume 32, pages 9154–9164, 2019.
- Hao Li, Zheng Xu, Gavin Taylor, Christoph Studer, and Tom Goldstein. Visualizing the loss landscape of neural nets. *Advances in neural information processing systems*, 31, 2018.
- J. Li, F. Li, and S. Todorovic. Efficient Riemannian optimization on the Stiefel manifold via the Cayley transform. In *International Conference on Learning Representations*, 2020a. arXiv:2002.01113.
- Jun Li, Fuxin Li, and Sinisa Todorovic. Efficient riemannian optimization on the Stiefel manifold via the Cayley transform. In *International Conference on Learning Representations (ICLR)*, 2020b.
- Alexandru Nica and Roland Speicher. *Lectures on the combinatorics of free probability*, volume 13. Cambridge University Press, 2006.
- J. Pennington, S. Schoenholz, and S. Ganguli. Resurrecting the sigmoid in deep learning through dynamical isometry: theory and practice. In *Advances in Neural Information Processing Systems*, volume 30, 2017.
- A. M. Saxe, J. L. McClelland, and S. Ganguli. Exact solutions to the nonlinear dynamics of learning in deep linear neural networks. *arXiv preprint arXiv:1312.6120*, 2014.
- S. S. Schoenholz, J. Gilmer, S. Ganguli, and J. Sohl-Dickstein. Deep information propagation. In *International Conference on Learning Representations*, 2017.
- Richard Sinkhorn. Diagonal equivalence to matrices with prescribed row and column sums. *The American Mathematical Monthly*, 74(4):402–405, 1967.
- R. Speicher. Combinatorial theory of the free product with amalgamation and operator-valued free probability theory. *Memoirs of the American Mathematical Society*, 132(627), 1998.
- Wojciech Tarnowski, Piotr Warchoł, Stanisław Jastrzębski, Jacek Tabor, and Maciej Nowak. Dynamical isometry is achieved in residual networks in a universal way for any activation function. In *The 22nd International Conference on Artificial Intelligence and Statistics*, pages 2221–2230. PMLR, 2019.
- Ashish Vaswani, Noam Shazeer, Niki Parmar, Jakob Uszkoreit, Llion Jones, Aidan N Gomez, Lukasz Kaiser, and Illia Polosukhin. Attention is all you need. In *Advances in Neural Information Processing Systems*, volume 30, 2017.
- C. Villani. *Topics in Optimal Transport*, volume 58 of *Graduate Studies in Mathematics*. American Mathematical Society, Providence, RI, 2003.
- D. Voiculescu. Operations on certain non-commutative operator-valued random variables. *Astérisque*, 232:243–275, 1995.
- Dan Voiculescu. Limit laws for random matrices and free products. *Inventiones mathematicae*, 104(1):201–220, 1991.
- Guoxin Wang, Jiaqi Li, Yifan Sun, Xiang Chen, Chang Liu, Yang Wu, Ming Lu, Shuqiang Song, and Yasin Abbasi Yadkori. Hierarchical reasoning model. *arXiv preprint arXiv:2506.21734*, 2025.
- H. Wang, S. Ma, L. Dong, S. Huang, D. Zhang, and F. Wei. DeepNet: Scaling transformers to 1,000 layers. *IEEE Transactions on Pattern Analysis and Machine Intelligence*, 2024. arXiv:2203.00555.

- S. Wisdom, T. Powers, J. Hershey, J. Le Roux, and L. Atlas. Full-capacity unitary recurrent neural networks. In *Advances in Neural Information Processing Systems*, volume 29, 2016.
- Zhenda Xie, Yixuan Wei, Huanqi Cao, Chenggang Zhao, Chengqi Deng, Jiashi Li, Damai Dai, Huazuo Gao, Jiang Chang, Kuai Yu, Liang Zhao, Shangyan Zhou, Zhean Xu, Zhengyan Zhang, Wangding Zeng, Shengding Hu, Yuqing Wang, Jingyang Yuan, Lean Wang, and Wenfeng Liang. mHC: Manifold-constrained hyper-connections. *arXiv preprint arXiv:2512.24880*, 2025.
- G. Yang and S. Schoenholz. Mean field residual networks: on the edge of chaos. In *Advances in Neural Information Processing Systems*, volume 30, 2017.
- Greg Yang. Tensor programs iii: Neural matrix laws. *arXiv preprint arXiv:2009.10685*, 2020.
- X. Yang and X. Gao. KromHC: Manifold-constrained hyper-connections with Kronecker-product residual matrices. *arXiv preprint arXiv:2601.21579*, 2026.
- Defa Zhu, Hongzhi Huang, Zihao Huang, Yutao Zeng, Yunyao Mao, Banggu Wu, Qiyang Min, and Xun Zhou. Hyper-connections. *arXiv preprint arXiv:2409.19606*, 2025. v2: 2512.24880.
- Z. Zhu, Y. He, L. Liu, J. Xu, Z. Xie, A. Dai, and D. Dai. Hyper-connections. *arXiv preprint arXiv:2409.19606*, 2024. Accepted at ICLR 2025.

A Matrices Manifolds

A.1 Doubly-Stochastic Matrices and the Birkhoff Polytope

Definition A.1 (Doubly-Stochastic Matrix). A matrix $\mathbf{P} \in \mathbb{R}^{n \times n}$ is doubly stochastic if $P_{ij} \geq 0$ for all i, j , $\mathbf{P}\mathbf{1} = \mathbf{1}$, and $\mathbf{P}^\top \mathbf{1} = \mathbf{1}$.

The set of all $n \times n$ doubly-stochastic matrices forms the *Birkhoff polytope* \mathcal{B}_n . By the Birkhoff-von Neumann theorem, \mathcal{B}_n is the convex hull of the $n!$ permutation matrices:

$$\mathcal{B}_n = \text{conv}\{\mathbf{P}_\sigma : \sigma \in S_n\}, \quad (15)$$

where $(\mathbf{P}_\sigma)_{ij} = \mathbb{1}[\sigma(j) = i]$.

A.2 Sinkhorn-Knopp Algorithm

The Sinkhorn-Knopp algorithm [Sinkhorn \[1967\]](#) projects an arbitrary non-negative matrix onto the Birkhoff polytope via alternating row and column normalization. In log-space (for numerical stability):

Algorithm 1 Sinkhorn-Knopp Projection (Log-Space)

Require: Unconstrained logit matrix $\mathbf{X} \in \mathbb{R}^{n \times n}$, iterations T

Ensure: Doubly-stochastic matrix $\mathbf{P} \in \mathcal{B}_n$

- 1: $\log \mathbf{M} \leftarrow \text{clamp}(\mathbf{X}, -10, 10)$
 - 2: **for** $t = 1, \dots, T$ **do**
 - 3: $\log \mathbf{M} \leftarrow \log \mathbf{M} - \text{LSE}_{\text{row}}(\log \mathbf{M})$ ▷ Row normalize
 - 4: $\log \mathbf{M} \leftarrow \log \mathbf{M} - \text{LSE}_{\text{col}}(\log \mathbf{M})$ ▷ Column normalize
 - 5: **end for**
 - 6: $\mathbf{P} \leftarrow \exp(\log \mathbf{M})$
 - 7: **return** \mathbf{P}
-

where $\text{LSE}_{\text{row}}(\mathbf{A})_{ij} = \log \sum_k \exp(A_{ik})$ broadcasts along rows.

B.2 Complete Cayley Transform

Algorithm 3 Iterative Cayley Transform

Require: Input matrix $\mathbf{H} \in \mathbb{R}^{B \times n \times n}$, step size α , iterations s

Ensure: Orthogonal matrix $\mathbf{Q} \in O(n)$

- 1: $\tilde{\mathbf{H}} \leftarrow \mathbf{H}.\text{view}(B, n, n)$
 - 2: $\mathbf{W} \leftarrow \tilde{\mathbf{H}} - \tilde{\mathbf{H}}^\top$ ▷ Skew-symmetrize
 - 3: $\mathbf{Y} \leftarrow \mathbf{I} + \alpha \mathbf{W}$ ▷ Initialize: $Y_0 = I + \alpha W$
 - 4: **for** $i = 1, \dots, s$ **do**
 - 5: $\mathbf{Y} \leftarrow \mathbf{I} + \frac{\alpha}{2} \mathbf{W}(\mathbf{I} + \mathbf{Y})$ ▷ Fixed-point iteration via `baddbmm`
 - 6: **end for**
 - 7: $\mathbf{Q} \leftarrow \mathbf{Y}$
 - 8: **return** \mathbf{Q}
-

B.3 Grassmannian Riemannian Step

Algorithm 4 Riemannian Gradient Step on $\text{Gr}(n, p)$

Require: Basis $\mathbf{U} \in \text{St}(n, p)$, Euclidean gradient ∇_E , momentum \mathbf{M}

Require: Step size α , momentum coefficient β_1

Ensure: Updated basis $\mathbf{U}' \in \text{St}(n, p)$

- 1: $\nabla_{\text{hor}} \leftarrow (\mathbf{I} - \mathbf{U}\mathbf{U}^\top)\nabla_E$ ▷ Horizontal (Riemannian) gradient
 - 2: $\mathbf{M} \leftarrow \beta_1 \mathbf{M} + (1 - \beta_1)\nabla_{\text{hor}}$ ▷ Momentum update
 - 3: $\mathbf{W} \leftarrow \mathbf{M}\mathbf{U}^\top - \mathbf{U}\mathbf{M}^\top$ ▷ Skew-symmetric generator
 - 4: $\mathbf{U}' \leftarrow \mathbf{U}$ ▷ Initialize Cayley retraction
 - 5: **for** $i = 1, \dots, s$ **do**
 - 6: $\mathbf{U}' \leftarrow \mathbf{U} + \frac{\alpha}{2} \mathbf{W}(\mathbf{U} + \mathbf{U}')$ ▷ Cayley retraction iteration
 - 7: **end for**
 - 8: **return** \mathbf{U}'
-

C Spectral Gap Computation Details

C.1 Algorithm for Exhaustive Spectral Gap Search

Algorithm 5 Exhaustive Search for Maximum Spectral Gap Generating Set

Require: Group order n , number of generators K

Ensure: Generating set $S^* \subseteq S_n$ with $|S^*| = K$ and maximum spectral gap

```

1:  $G \leftarrow S_n$  ▷ Symmetric group on  $n$  elements
2: elements  $\leftarrow \text{list}(G)$ ,  $N \leftarrow |G| = n!$ 
3:  $\Delta^* \leftarrow 0$ ,  $S^* \leftarrow \emptyset$ 
4: for each  $S \subseteq G$  with  $|S| = K$  do
5:   if  $S$  does not generate  $G$  via BFS closure then
6:     continue
7:   end if
8:    $\mathbf{T} \leftarrow \mathbf{0}^{N \times N}$  ▷ Transition matrix
9:   for  $g \in G$ ,  $\sigma \in S$  do
10:     $\mathbf{T}[g, g\sigma] += 1/K$  ▷ Right-multiplication walk
11:   end for
12:    $\lambda_1, \lambda_2, \dots \leftarrow \text{eigenvalues}(\mathbf{T})$ , sorted by  $|\lambda|$ 
13:    $\Delta \leftarrow |\lambda_1| - |\lambda_2|$ 
14:   if  $\Delta > \Delta^*$  then
15:      $\Delta^* \leftarrow \Delta$ ,  $S^* \leftarrow S$ 
16:   end if
17: end for
18: return  $S^*$ ,  $\Delta^*$ 

```

C.2 Complexity Analysis

For n streams and K generators:

- Number of candidate subsets: $\binom{n!}{K}$
- BFS closure check: $\mathcal{O}(n! \cdot K)$ per subset
- Eigendecomposition: $\mathcal{O}((n!)^3)$ per valid generating set
- Total: $\mathcal{O}\left(\binom{n!}{K} \cdot (n!)^3\right)$

Table 7: Tractability of exhaustive spectral gap search.

n	$n!$	$\binom{n!}{4}$	Matrix size	Feasibility
3	6	15	6×6	$< 0.01\text{s}$
4	24	10,626	24×24	$\sim 0.3\text{s}$
5	120	8,214,570	120×120	$\sim 1 \text{ hour}$
6	720	$\sim 10^{10}$	720×720	Intractable

D JPmHC Module Parameter Counts

With 4 unique JPmHC modules per model (2 per unique layer, weight-tied across 6 recursive cycles), the total JPmHC parameter overhead ranges from $\sim 115\text{K}$ (Perm Mix) to $\sim 410\text{K}$ (Cayley), which is 1.6–5.8% of the $\sim 7\text{M}$ total model parameters.

Table 8: Parameter count per JpMHC module ($n = 4$, $d = 512$, $nd = 2048$).

Variant	D_{res}	Total params	Notes
Sinkhorn	$n^2 = 16$	$(n + n + 16) \times nd + 36 = 49,188$	Fused ϕ
Cayley	$3n^2 = 48$	$48 \times nd + \text{LayerNorm} = 102,400$	Fused $\phi + \text{LN}$
Grassmann	$np = 8$	$(n + n + 8) \times nd + 28 = 32,796$	$p = 2$
Perm Mix	$K = 6$	$(n + n + 6) \times nd + 22 = 28,694$	+ perm indices

E Convergence of Gauss-Seidel Solver

The convergence rate of the Gauss-Seidel solver for the implicit Sinkhorn backward depends on the spectral radius ρ of the iteration matrix. For a doubly-stochastic matrix \mathbf{P} with entries bounded away from 0 and 1, the spectral radius satisfies $\rho < 1$, ensuring convergence.

Table 9: Gauss-Seidel convergence for $n = 4$ with typical \mathbf{P} matrices.

Iterations k	Relative residual $\ \mathbf{r}\ /\ \mathbf{r}_0\ $	Gradient error (%)
1	7.5×10^{-1}	43.2
2	5.6×10^{-1}	28.1
4	3.2×10^{-1}	11.5
8	1.0×10^{-1}	2.8
16	1.0×10^{-2}	0.08
32	1.0×10^{-4}	< 0.001

Our default of $k = 4n = 16$ iterations achieves < 0.1% gradient error, which is sufficient for stable training with standard learning rates.

F Derivation of Dyson Equation for mHC

We derive the generalized Green’s function governing the singular value spectrum of random matrices of the form $Y = A + X$, where A is deterministic and X is an isotropic random matrix. Using a block linearization and a resolvent expansion, we prove a matrix Dyson equation (Schwinger–Dyson / Pastur equation) for a deterministic equivalent resolvent. Isotropy forces the self-energy to collapse to scalar multiples of the identity, reducing the spectral analysis to a small set of order parameters.

F.1 Problem Setup

Let

$$Y = A + X \in \mathbb{R}^{N \times N},$$

where A is deterministic and X is centered random. We study singular values of Y via

$$S := YY^\top.$$

For $z \in \mathbb{C}^+$ define the Stieltjes transform

$$G_S(z) = \frac{1}{N} \text{Tr}(zI - S)^{-1}.$$

We will access G_S through a block linearization.

F.2 Block Linearization

Define the $2N \times 2N$ matrix

$$\mathcal{L}(z) = \begin{pmatrix} zI & -Y \\ -Y^\top & I \end{pmatrix}.$$

Schur complement. The $(1, 1)$ block of $\mathcal{L}(z)^{-1}$ equals the desired resolvent:

$$(\mathcal{L}(z)^{-1})_{11} = (zI - YY^\top)^{-1}.$$

Hence

$$G_S(z) = \frac{1}{N} \text{Tr}(\mathcal{L}(z)^{-1})_{11}.$$

F.3 Generalized Green's Function

For a block matrix

$$M = \begin{pmatrix} M_{11} & M_{12} \\ M_{21} & M_{22} \end{pmatrix} \in \mathbb{R}^{2N \times 2N},$$

define the block trace

$$\text{bTr}(M) = \begin{pmatrix} \frac{1}{N} \text{Tr}(M_{11}) & \frac{1}{N} \text{Tr}(M_{12}) \\ \frac{1}{N} \text{Tr}(M_{21}) & \frac{1}{N} \text{Tr}(M_{22}) \end{pmatrix}.$$

Define the generalized Green's function

$$\mathcal{G}(z) = \text{bTr} \mathbb{E}[\mathcal{L}(z)^{-1}] = \begin{pmatrix} g_{11} & g_{12} \\ g_{21} & g_{22} \end{pmatrix}.$$

Then $G_S(z) = g_{11}(z)$.

F.4 Isotropy Assumption

We assume X is isotropic in the second-moment sense: there exists $\sigma^2 > 0$ such that

$$\boxed{\mathbb{E}[XBX^\top] = \frac{\sigma^2}{N} \text{Tr}(B) I} \quad \text{for every deterministic } B \in \mathbb{R}^{N \times N}.$$

This holds for i.i.d. Gaussian $X_{ij} \sim \mathcal{N}(0, \sigma^2/N)$ and more generally for left-right orthogonally invariant ensembles with the same covariance.

F.5 Resolvent, Resolvent Identity, and the Dyson Equation

This section expands the resolvent machinery and proves the Dyson equation used later.

F.5.1 Definition of the resolvent

For any (square) matrix $H \in \mathbb{R}^{m \times m}$ and any $w \in \mathbb{C}$ not in the spectrum of H , the *resolvent* is

$$R_H(w) := (wI_m - H)^{-1}.$$

In our setting, the primary object is the *block resolvent* of $\mathcal{L}(z)$:

$$\mathcal{R}(z) := \mathcal{L}(z)^{-1}.$$

When we split $\mathcal{L}(z)$ into a deterministic part and a random perturbation, we also use the *bare resolvent*

$$\mathcal{R}_0(z) := \mathcal{L}_0(z)^{-1}.$$

F.5.2 Splitting into deterministic and random parts

Write

$$\mathcal{L}(z) = \underbrace{\begin{pmatrix} zI & -A \\ -A^\top & I \end{pmatrix}}_{=: \mathcal{L}_0(z)} - \underbrace{\begin{pmatrix} 0 & X \\ X^\top & 0 \end{pmatrix}}_{=: \mathcal{X}}.$$

Thus $\mathcal{L} = \mathcal{L}_0 - \mathcal{X}$.

F.5.3 Resolvent identity (exact)

The following is a standard identity.

Lemma (resolvent identity). If B is invertible and C is arbitrary such that $B - C$ is invertible, then

$$(B - C)^{-1} = B^{-1} + B^{-1}C(B - C)^{-1}.$$

Proof. Multiply the right-hand side by $(B - C)$:

$$(B^{-1} + B^{-1}C(B - C)^{-1})(B - C) = I + B^{-1}C - B^{-1}C = I.$$

Hence it equals $(B - C)^{-1}$. □

Apply this with $B = \mathcal{L}_0$ and $C = \mathcal{X}$:

$$\mathcal{R} = \mathcal{R}_0 + \mathcal{R}_0 \mathcal{X} \mathcal{R}. \tag{19}$$

Taking expectation (and using that \mathcal{R}_0 is deterministic),

$$\mathbb{E}[\mathcal{R}] = \mathcal{R}_0 + \mathcal{R}_0 \mathbb{E}[\mathcal{X} \mathcal{R}]. \tag{20}$$

Equation (20) is exact but not closed because $\mathbb{E}[\mathcal{X} \mathcal{R}]$ depends on correlations between \mathcal{X} and \mathcal{R} .

F.5.4 Dyson equation via a self-energy (Gaussian / Wick closure)

To close (20), one introduces the *self-energy* operator $\Sigma[\cdot]$. For Gaussian (or Wick-type) ensembles, the closure is governed by second moments.

We state a standard large- N closure (often proved with Gaussian integration by parts / Stein's lemma, or with cumulant expansions and planar diagrammatics). We use it here as the key computational step.

Assumption (Gaussian/Wick closure). Assume X has entries with variance σ^2/N and satisfies Wick's rule (e.g. i.i.d. Gaussian). Then for resolvents \mathcal{R} , the leading-order contribution to $\mathbb{E}[\mathcal{X} \mathcal{R}]$ can be written as

$$\mathbb{E}[\mathcal{X} \mathcal{R}] = \Sigma[\mathbb{E}[\mathcal{R}]] \mathbb{E}[\mathcal{R}] + o_N(1),$$

in an entrywise or normalized-trace sense (depending on the regularity assumptions).

Under this closure, (20) becomes

$$\mathbb{E}[\mathcal{R}] \approx \mathcal{R}_0 + \mathcal{R}_0 \Sigma[\mathbb{E}[\mathcal{R}]] \mathbb{E}[\mathcal{R}].$$

Rearranging,

$$(\mathcal{R}_0^{-1} - \Sigma[\mathbb{E}[\mathcal{R}]]) \mathbb{E}[\mathcal{R}] \approx I,$$

hence

$$\mathbb{E}[\mathcal{R}] \approx (\mathcal{L}_0 - \Sigma[\mathbb{E}[\mathcal{R}]])^{-1}.$$

This motivates defining a deterministic equivalent $\mathcal{M}(z)$ as the solution to the *matrix Dyson equation*:

$$\boxed{\mathcal{M}(z) = (\mathcal{L}_0(z) - \Sigma[\mathcal{M}(z)])^{-1}.} \quad (21)$$

In many models (including i.i.d. Gaussian), one can show $\mathbb{E}[\mathcal{R}(z)] - \mathcal{M}(z) \rightarrow 0$ in normalized trace, uniformly for $\text{Im}(z) \geq \eta > 0$.

F.5.5 Computing the self-energy under isotropy

Let

$$\mathcal{M} = \begin{pmatrix} M_{11} & M_{12} \\ M_{21} & M_{22} \end{pmatrix}.$$

Because \mathcal{X} is off-diagonal, $\Sigma[\mathcal{M}]$ is also off-diagonal at leading order. Under isotropy, the contraction identities imply:

$$\mathbb{E}[X M_{21} X^\top] = \frac{\sigma^2}{N} \text{Tr}(M_{21}) I, \quad \mathbb{E}[X^\top M_{12} X] = \frac{\sigma^2}{N} \text{Tr}(M_{12}) I.$$

This yields the self-energy map

$$\boxed{\Sigma[\mathcal{M}] = \begin{pmatrix} 0 & \sigma^2 m_{12} I \\ \sigma^2 m_{21} I & 0 \end{pmatrix}, \quad m_{12} := \frac{1}{N} \text{Tr}(M_{12}), \quad m_{21} := \frac{1}{N} \text{Tr}(M_{21}).}$$

Therefore, even for general deterministic A , isotropy collapses the random correction to scalar multiples of the identity, reducing the random-matrix effect to two scalar order parameters.

F.6 Closed Dyson Equation and Order Parameters

Combining (21) with the isotropic self-energy gives

$$\mathcal{M}^{-1} = \begin{pmatrix} zI & -A \\ -A^\top & I \end{pmatrix} - \begin{pmatrix} 0 & \sigma^2 m_{12} I \\ \sigma^2 m_{21} I & 0 \end{pmatrix},$$

i.e.

$$\mathcal{M}^{-1} = \begin{pmatrix} zI & -(A + \sigma^2 m_{12} I) \\ -(A^\top + \sigma^2 m_{21} I) & I \end{pmatrix}.$$

The order parameters satisfy the self-consistency equations

$$m_{12} = \frac{1}{N} \text{Tr}(M_{12}), \quad m_{21} = \frac{1}{N} \text{Tr}(M_{21}).$$

Finally,

$$G_S(z) \approx \frac{1}{N} \text{Tr} M_{11}(z).$$

F.7 Special Case: Scalar Skip Connection

If $A = aI$, then the Dyson equation collapses from $2N \times 2N$ to a 2×2 system because all blocks commute and M_{ij} are scalar multiples of I .

F.8 Conceptual Takeaway

The key mechanism is:

1. linearize YY^\top into a $2N \times 2N$ operator,
2. write the exact resolvent identity,
3. close it via Wick contractions into a Dyson equation,
4. use isotropy to reduce the self-energy to scalars $\times I$.

This identifies the minimal set of order parameters controlling the singular spectrum of $Y = A + X$.

G Training and Architecture Details

G.1 TRM Architecture Configuration

Table 10: Full TRM architecture configuration.

Parameter	Value
Total parameters	$\sim 7\text{M}$
Hidden dimension d	512
Number of streams n	4
Effective hidden dim nd	2048
Unique transformer layers (weight-tied)	2
Recursive cycles per layer	6
Total recursive applications	12
Attention heads	8
FFN expansion ratio	$4\times$
Halting mechanism	Adaptive Computation Time (ACT)
ACT max recursion depth	16
ACT exploration probability	0.1
JPmHC modules per layer	2 (pre-attention, pre-FFN)
Total JPmHC modules	4 (shared via weight tying)
Positional encoding	RoPE
Flash Attention	Enabled (with SDPA fallback)

G.2 Training Hyperparameters

AdamAtan2 Optimizer. AdamAtan2 replaces the standard Adam update $m_t/(\sqrt{v_t} + \epsilon)$ with $\text{atan2}(m_t, \sqrt{v_t})$, providing more stable gradient scaling and eliminating sensitivity to the ϵ hyperparameter. For the Grassmann variant, we additionally employ a `GrassmannianOptimizer` wrapper that applies Riemannian gradient steps to the subspace basis parameters \mathbf{U} .

DeepSpeed compatibility. Although our framework supports DeepSpeed ZeRO-2/ZeRO-3, profiling showed that for 7M parameters, vanilla DDP with `torch.compile` is faster due to lower communication overhead. All JPmHC variants are validated compatible with both backends.

Table 11: Training hyperparameters (shared across all variants).

Hyperparameter	Value
Optimizer	AdamAtan2 [Kunstner et al., 2023]
Learning rate	1×10^{-4}
Global batch size	768
Weight decay	0.1
Gradient clipping	1.0
LR schedule	Step decay at 80% and 90% of training
LR decay factors	0.316 \times and 0.1 \times
Warmup steps	2000
Precision	bfloat16 (mixed precision)
Framework	PyTorch DDP + <code>torch.compile</code>
Compile mode	<code>default</code>
Hardware	NVIDIA B200 192GB GPUs ($\times 8$)
Puzzle embedding optimizer	SignSGD (lr= 10^{-2})
Puzzle embedding dim	512 ($\times 16$ tokens)

G.3 Permutation Basis Construction

For the Perm Mix variant with $n = 4$ streams and $K = 6$ permutations, the default permutation basis is:

1. **Identity** e : (0, 1, 2, 3)
2. **Adjacent transpositions**: (1, 0, 2, 3), (0, 1, 3, 2)
3. **Cyclic shifts**: (1, 2, 3, 0), (3, 0, 1, 2)
4. **Random fill** (seed 42): remaining permutations sampled to reach $K = 6$

This basis includes generators of S_4 (adjacent transpositions generate the full symmetric group) while adding cyclic structure for efficient mixing.

H Sinkhorn Variant with Implicit Differentiation

The Sinkhorn variant projects the residual mixing matrix \mathbf{H}_{res} onto the Birkhoff polytope \mathcal{B}_n of doubly-stochastic matrices. Our key contribution is a custom backward pass that eliminates the autograd graph explosion of the standard Sinkhorn-Knopp implementation.

H.1 Problem: Autograd Graph Explosion

The standard implementation records all T Sinkhorn iterations in the PyTorch autograd graph. Each iteration involves two log-sum-exp operations, each of which PyTorch decomposes into multiple elementary ops (exp, sum, log, subtract). For $T = 20$ iterations on $n \times n = 4 \times 4$ matrices, this creates approximately 128,000 backward nodes.

These nodes produce only *microsecond-scale* GPU kernels—far too small to overlap with DDP AllReduce communication. Our profiling on NVIDIA B200 GPUs revealed that 55% of the total backward pass time was spent on DDP synchronization stalls, waiting for AllReduce operations to complete because no substantial compute was available to overlap with them.

H.2 Solution: Custom Autograd Function with Implicit Differentiation

We implement a custom `torch.autograd.Function` that decouples the forward and backward passes:

Forward Pass. The Sinkhorn iterations run under `torch.no_grad()`, so no autograd graph is recorded. Only the final doubly-stochastic matrix \mathbf{P} is saved for the backward pass:

Algorithm 6 Implicit Sinkhorn — Forward Pass

Require: Logit matrix $\mathbf{X} \in \mathbb{R}^{n \times n}$, iterations T

Ensure: $\mathbf{P} \in \mathcal{B}_n$ (doubly-stochastic)

- 1: **with** `torch.no_grad()`: ▷ No autograd recording
 - 2: $\log \mathbf{M} \leftarrow \text{clamp}(\mathbf{X}, -10, 10)$
 - 3: **for** $t = 1, \dots, T$ **do**
 - 4: $\log \mathbf{M} \leftarrow \log \mathbf{M} - \text{LSE}_{\text{row}}(\log \mathbf{M})$
 - 5: $\log \mathbf{M} \leftarrow \log \mathbf{M} - \text{LSE}_{\text{col}}(\log \mathbf{M})$
 - 6: **end for**
 - 7: $\mathbf{P} \leftarrow \exp(\log \mathbf{M})$
 - 8: **save** \mathbf{P} for backward
 - 9: **return** \mathbf{P}
-

Backward Pass. Gradients are computed via implicit differentiation of the fixed-point conditions, following the framework of Eisenberger et al. [Eisenberger et al. \[2022b\]](#). At the doubly-stochastic fixed point, the constraints are:

$$\mathbf{P}\mathbf{1} = \mathbf{1} \quad \text{and} \quad \mathbf{P}^\top \mathbf{1} = \mathbf{1}. \quad (22)$$

Proposition H.1 (Implicit Sinkhorn Gradient [Eisenberger et al. \[2022b\]](#)). *Let $\mathbf{P} = \Pi_{\mathcal{B}}(\mathbf{X})$ be the Sinkhorn projection of \mathbf{X} onto the Birkhoff polytope. Given the upstream gradient $\nabla_{\mathbf{P}} \mathcal{L}$, the gradient with respect to the input is:*

$$\frac{\partial \mathcal{L}}{\partial \mathbf{X}} = \mathbf{P} \odot \left(\nabla_{\mathbf{P}} \mathcal{L} - \mathbf{u}\mathbf{1}^\top - \mathbf{1}\mathbf{v}^\top \right), \quad (23)$$

where $\mathbf{u} \in \mathbb{R}^{n \times 1}$ and $\mathbf{v} \in \mathbb{R}^{1 \times n}$ solve the coupled linear system:

$$\mathbf{P}\mathbf{v}^\top + \mathbf{u} = \mathbf{h}_{\text{row}}, \quad (24)$$

$$\mathbf{P}^\top \mathbf{u} + \mathbf{v}^\top = \mathbf{h}_{\text{col}}, \quad (25)$$

with

$$\mathbf{h}_{\text{row}} = (\mathbf{P} \odot \nabla_{\mathbf{P}} \mathcal{L})\mathbf{1}, \quad \mathbf{h}_{\text{col}} = \mathbf{1}^\top (\mathbf{P} \odot \nabla_{\mathbf{P}} \mathcal{L}). \quad (26)$$

H.3 Gauss-Seidel Solver for the Coupled System

The coupled system (24)–(25) can be solved efficiently via Gauss-Seidel iteration. Starting from $\mathbf{v}^{(0)} = \mathbf{0}$:

Algorithm 7 Implicit Sinkhorn — Backward Pass (Gauss-Seidel)

Require: Saved $\mathbf{P} \in \mathcal{B}_n$, upstream gradient $\nabla_{\mathbf{P}}\mathcal{L}$

Ensure: $\nabla_{\mathbf{X}}\mathcal{L}$

```
1:  $\mathbf{H} \leftarrow \mathbf{P} \odot \nabla_{\mathbf{P}}\mathcal{L}$  ▷ Elementwise product
2:  $\mathbf{h}_{\text{row}} \leftarrow \mathbf{H}\mathbf{1}$  ▷ Row sums, shape  $(\dots, n, 1)$ 
3:  $\mathbf{h}_{\text{col}} \leftarrow \mathbf{1}^\top \mathbf{H}$  ▷ Column sums, shape  $(\dots, 1, n)$ 
4:  $k \leftarrow \text{GAUSSSEIDELITERS}(n)$  ▷ See Proposition H.2
5:  $\mathbf{v} \leftarrow \mathbf{0}$  ▷ Shape  $(\dots, 1, n)$ 
6: for  $i = 1, \dots, k$  do
7:    $\mathbf{u} \leftarrow \mathbf{h}_{\text{row}} - \mathbf{P}\mathbf{v}^\top$  ▷ Shape  $(\dots, n, 1)$ 
8:    $\mathbf{v} \leftarrow \mathbf{h}_{\text{col}} - (\mathbf{P}^\top \mathbf{u})^\top$  ▷ Shape  $(\dots, 1, n)$ 
9: end for
10:  $\nabla_{\mathbf{X}}\mathcal{L} \leftarrow \mathbf{H} - \mathbf{u} \odot \mathbf{P} - \mathbf{v} \odot \mathbf{P}$ 
11: return  $\nabla_{\mathbf{X}}\mathcal{L}$ 
```

H.4 Convergence Analysis

Proposition H.2 (Gauss-Seidel Convergence Rate). *For the coupled linear system arising from an $n \times n$ doubly-stochastic matrix \mathbf{P} , the spectral radius of the Gauss-Seidel iteration matrix is bounded by:*

$$\rho \leq 1 - \frac{1}{n}. \quad (27)$$

To achieve a relative residual $\epsilon \leq 0.01$, the required number of iterations is:

$$k \geq \left\lceil \frac{\log \epsilon}{\log \rho} \right\rceil = \left\lceil \frac{\log 0.01}{\log(1 - 1/n)} \right\rceil. \quad (28)$$

This yields the following iteration counts for practical values of n :

Table 12: Required Gauss-Seidel iterations for $\epsilon = 0.01$ convergence.

n	2	3	4	5	6	8
$\rho = 1 - 1/n$	0.500	0.667	0.750	0.800	0.833	0.875
Iterations k	7	12	16	21	26	37

For our production configuration with $n = 4$ streams, $k = 16$ Gauss-Seidel iterations suffice. We enforce bounds $k \in [10, 50]$ as a safety net.

H.5 Self-Stabilization Property

An important property of the implicit gradient formula (23) is its **self-stabilization**: the factor $\mathbf{P} \odot (\cdot)$ ensures that entries where $P_{ij} \approx 0$ automatically produce near-zero gradients, regardless of the accuracy of \mathbf{u} and \mathbf{v} . This means no clamping of \mathbf{P} is needed in the backward pass, and the formula is robust to numerical precision issues in the Sinkhorn forward iterations.

Remark H.3. *Empirically, we verified that clamped ($P_{ij} \geq 10^{-8}$) and unclamped versions produce identical gradients (cosine similarity difference $< 10^{-6}$) across all tested gradient magnitudes.*

H.6 Fused Projection Optimization

All three mapping projections ($\phi_{\text{pre}}, \phi_{\text{post}}, \phi_{\text{res}}$) are computed via a single fused linear layer:

$$[\phi_{\text{pre}} \mid \phi_{\text{post}} \mid \phi_{\text{res}}] = \mathbf{W}_{\text{fused}} \cdot \text{RMSNORM}(\mathbf{x}_{\text{flat}}), \quad (29)$$

where $\mathbf{W}_{\text{fused}} \in \mathbb{R}^{(n+n+n^2) \times nd}$. This reads the input tensor once instead of three times, reducing memory bandwidth by $\sim 3\times$ and cutting kernel launch overhead from 3 to 1.

H.7 Complexity Comparison

Table 13: Backward pass complexity: standard vs. implicit Sinkhorn.

	Standard Sinkhorn	Implicit Sinkhorn (Ours)
Autograd nodes	$\mathcal{O}(T \cdot n^2)$ ($\sim 128\text{K}$)	$\mathcal{O}(1)$ (constant)
Backward kernels	$\sim 128\text{K}$ microsecond-scale	~ 20 millisecond-scale
DDP overlap	Poor (55% stalls)	Excellent
Memory (saved tensors)	$\mathcal{O}(T \cdot n^2)$	$\mathcal{O}(n^2)$ (just \mathbf{P})
Gradient accuracy	Exact	$\epsilon \leq 0.01$ (controlled)

I Cayley Transform Variant

The Cayley variant replaces the doubly-stochastic constraint (Birkhoff polytope) with the *orthonormality* constraint (Stiefel manifold). Instead of requiring $\mathbf{H}_{\text{res}}^\top \mathbf{1} = \mathbf{1}$ and $\mathbf{H}_{\text{res}} \mathbf{1} = \mathbf{1}$, we require $\mathbf{H}_{\text{res}}^\top \mathbf{H}_{\text{res}} = \mathbf{I}_n$, which provides **norm-preserving** stream mixing: $\|\mathbf{H}_{\text{res}} \mathbf{x}\| = \|\mathbf{x}\|$.

I.1 Mathematical Formulation

The Cayley transform (18) maps skew-symmetric matrices $\mathbf{W} = -\mathbf{W}^\top$ to orthogonal matrices. However, the closed-form requires a matrix inverse $(\mathbf{I} - \mathbf{W}/2)^{-1}$, which is computationally expensive for batched computation and not amenable to GPU parallelism. Following Li et al. [2020b], we use an iterative approximation.

I.2 Iterative Cayley Transform

Given an unconstrained matrix $\tilde{\mathbf{H}} \in \mathbb{R}^{n \times n}$, the projection proceeds in three steps:

Step 1: Skew-Symmetrization. Ensure the input lies in the Lie algebra of $O(n)$:

$$\mathbf{W} = \tilde{\mathbf{H}} - \tilde{\mathbf{H}}^\top. \quad (30)$$

This guarantees $\mathbf{W} = -\mathbf{W}^\top$, which is necessary for the Cayley transform to map to $O(n)$.

Step 2: Initialization. Since we start from the identity ($\mathbf{X} = \mathbf{I}_n$), the initial estimate simplifies:

$$\mathbf{Y}_0 = \mathbf{I}_n + \alpha \mathbf{W}, \quad (31)$$

where $\alpha > 0$ is a step-size parameter (default $\alpha = 0.1$). This saves one matrix multiplication compared to the general case $\mathbf{Y}_0 = \mathbf{X} + \alpha \mathbf{W}\mathbf{X}$.

Step 3: Fixed-Point Iteration. The iterate converges to the Cayley retraction:

$$\mathbf{Y}_{i+1} = \mathbf{I}_n + \frac{\alpha}{2} \mathbf{W}(\mathbf{I}_n + \mathbf{Y}_i), \quad i = 0, 1, \dots, s-1. \quad (32)$$

The full algorithm is:

Algorithm 8 Iterative Cayley Transform Projection

Require: Unconstrained matrix $\tilde{\mathbf{H}} \in \mathbb{R}^{n \times n}$, step-size α , iterations s

Ensure: Approximately orthonormal matrix $\mathbf{Y} \in \mathbb{R}^{n \times n}$ ($\mathbf{Y}^\top \mathbf{Y} \approx \mathbf{I}$)

```
1:  $\mathbf{W} \leftarrow \tilde{\mathbf{H}} - \tilde{\mathbf{H}}^\top$  ▷ Skew-symmetrize
2:  $\mathbf{Y} \leftarrow \mathbf{I}_n + \alpha \mathbf{W}$  ▷ Initialize (saves one matmul since  $\mathbf{X} = \mathbf{I}$ )
3: for  $i = 1, \dots, s$  do
4:    $\mathbf{Y} \leftarrow \mathbf{I}_n + \frac{\alpha}{2} \mathbf{W}(\mathbf{I}_n + \mathbf{Y})$  ▷ Fixed-point step via baddbmm
5: end for
6: return  $\mathbf{Y}$ 
```

I.3 Properties of the Cayley Projection

Proposition I.1 (Norm Preservation). *For \mathbf{Y} produced by Algorithm 8, $\|\mathbf{Y}\mathbf{x}\| \approx \|\mathbf{x}\|$ for all $\mathbf{x} \in \mathbb{R}^n$, with the approximation improving with more iterations s .*

Proposition I.2 (Determinant). *The determinant satisfies $|\det(\mathbf{Y})| \approx 1$, approaching exactness as $s \rightarrow \infty$.*

In practice, $s = 2$ iterations suffice for deep learning applications Li et al. [2020b], achieving orthonormality deviation $\|\mathbf{Y}^\top \mathbf{Y} - \mathbf{I}\|_{\max} < 10^{-3}$.

I.4 CUDA Graph Compatibility

A critical implementation detail is **pre-allocation of the identity matrix**. When using `torch.compile(mode='reduce-overhead')`, PyTorch captures CUDA graphs that require static tensor shapes. Dynamic calls to `torch.eye()` or `torch.ones()` during forward pass break graph capture.

We solve this by registering the identity matrix as a persistent buffer during module initialization:

```
self.register_buffer("_identity", torch.eye(n), persistent=False) (33)
```

For batched operation (when the batch size $B \cdot L$ is known), we pre-expand:

```
 $\mathbf{I}_{\text{batch}} = \mathbf{I}_n.\text{unsqueeze}(0).\text{expand}(B \cdot L, n, n).\text{contiguous}().$  (34)
```

This ensures the same memory is reused across forward passes, enabling CUDA graph capture.

I.5 Layer Architecture

The full Cayley JPMHC layer computes three mapping matrices per token:

1. **Fused projection:** A single linear layer produces all three unconstrained matrices:

$$[\tilde{\mathbf{H}}_{\text{pre}} \mid \tilde{\mathbf{H}}_{\text{post}} \mid \tilde{\mathbf{H}}_{\text{res}}] = \mathbf{W}_{\text{fused}} \cdot \text{LayerNorm}(\mathbf{x}_{\text{flat}}), \quad (35)$$

where $\mathbf{W}_{\text{fused}} \in \mathbb{R}^{3n^2 \times nd}$ and the output is split and reshaped to $(B \cdot L, n, n)$ for each.

2. **Constraint projection:**

$$\mathbf{H}_{\text{pre}} = \text{softmax}(\tilde{\mathbf{H}}_{\text{pre}}/\tau, \text{dim} = -1), \quad (36)$$

$$\mathbf{H}_{\text{post}} = \text{softmax}(\tilde{\mathbf{H}}_{\text{post}}/\tau, \text{dim} = -2), \quad (37)$$

$$\mathbf{H}_{\text{res}} = \text{Cay}_{\text{iter}}(\tilde{\mathbf{H}}_{\text{res}}). \quad (38)$$

Note that \mathbf{H}_{pre} and \mathbf{H}_{post} use softmax (row-stochastic and column-stochastic respectively, with temperature τ) rather than sigmoid, since the Cayley variant operates on full $n \times n$ mixing matrices for pre/post.

3. Forward computation:

$$\mathbf{x}_{\text{pre}} = \mathbf{H}_{\text{pre}} \cdot \mathbf{x}_{\text{streams}}, \quad (39)$$

$$\mathbf{x}_{\text{in}} = \text{mean}(\mathbf{x}_{\text{pre}}, \text{dim} = \text{stream}), \quad (40)$$

$$\mathbf{y} = F(\mathbf{x}_{\text{in}}), \quad (41)$$

$$\mathbf{y}_{\text{streams}} = s \cdot \mathbf{H}_{\text{post,sum}} \odot \mathbf{y}, \quad (42)$$

$$\mathbf{x}_{\text{out}} = \mathbf{H}_{\text{res}} \cdot \mathbf{x}_{\text{streams}} + \mathbf{y}_{\text{streams}}. \quad (43)$$

The final combination uses `torch.baddbmm` for a fused residual-plus-write operation, avoiding a separate `bmm` followed by addition.

I.6 Comparison: Doubly-Stochastic vs. Orthonormal Mixing

Table 14: Properties of doubly-stochastic (Sinkhorn) vs. orthonormal (Cayley) mixing.

Property	Doubly-Stochastic (\mathcal{B}_n)	Orthonormal ($O(n)$)
Norm behavior	Contractive ($\ \mathbf{H}\mathbf{x}\ \leq \ \mathbf{x}\ $)	Preserving ($\ \mathbf{H}\mathbf{x}\ = \ \mathbf{x}\ $)
Entries	Non-negative	Unconstrained sign
Row/col sums	Both equal $\mathbf{1}$	Not constrained
$\det(\mathbf{H})$	$\in [0, 1]$	± 1
Convex hull	Permutation matrices	Not a convex set
Gradient flow	May attenuate	Preserved
Backward cost	$\mathcal{O}(T)$ or implicit	Standard autograd

The norm-preserving property of orthonormal mixing is particularly beneficial for recursive models where the same layer is applied multiple times—it prevents representation collapse or explosion across recursion steps.

J Grassmannian Variant

The Grassmannian variant provides a **parameter-efficient** alternative to both Sinkhorn and Cayley by learning a rank- p subspace projection instead of a full $n \times n$ mixing matrix. The residual mapping is represented as:

$$\mathbf{H}_{\text{res}} = \mathbf{U}\mathbf{U}^\top, \quad \mathbf{U} \in \text{St}(n, p), \quad \mathbf{U}^\top \mathbf{U} = \mathbf{I}_p, \quad (44)$$

where $p \leq n$ (default $p = \lfloor n/2 \rfloor$). This projector is **idempotent** ($\mathbf{H}_{\text{res}}^2 = \mathbf{H}_{\text{res}}$), **symmetric** ($\mathbf{H}_{\text{res}} = \mathbf{H}_{\text{res}}^\top$), and has **rank exactly** p .

J.1 Parameter Efficiency

The key advantage is the reduction in parameters for the residual mixing:

Table 15: Parameter count for residual mixing matrix ($n = 4$).

Variant	Parameters	$n = 4$
Sinkhorn (full $n \times n$)	n^2	16
Cayley (full $n \times n$)	n^2	16
Grassmannian ($n \times p$, $p = n/2$)	np	8

While the savings are modest for $n = 4$, they become significant for larger n and when accumulated across all layers in a recursive model.

J.2 Riemannian Optimization via Cayley ADAM

Standard gradient descent in Euclidean space does not preserve the Stiefel constraint $\mathbf{U}^\top \mathbf{U} = \mathbf{I}_p$. We employ a full Riemannian optimization scheme that combines **horizontal projection**, **momentum**, and **Cayley retraction**.

J.2.1 Step 1: Horizontal Projection

On the Grassmann manifold $\text{Gr}(n, p) = \text{St}(n, p)/O(p)$, the tangent space at \mathbf{U} decomposes into:

$$T_{\mathbf{U}}\text{St}(n, p) = \underbrace{T_{\mathbf{U}}^{\text{hor}}}_{\text{horizontal}} \oplus \underbrace{T_{\mathbf{U}}^{\text{ver}}}_{\text{vertical (fiber)}}. \quad (45)$$

The vertical space corresponds to rotations *within* the subspace (i.e., right multiplication by $O(p)$), which do not change the projector $\mathbf{U}\mathbf{U}^\top$. The horizontal projection removes this component:

$$\nabla_{\text{hor}} = (\mathbf{I}_n - \mathbf{U}\mathbf{U}^\top)\nabla_{\text{eucl}} = \nabla_{\text{eucl}} - \mathbf{U}(\mathbf{U}^\top \nabla_{\text{eucl}}). \quad (46)$$

This is essential for Grassmannian (as opposed to Stiefel) optimization: it ensures we move in directions that actually change the subspace, not just rotate the basis within it.

J.2.2 Step 2: Cayley ADAM Momentum

We maintain exponential moving averages of the horizontally-projected gradient:

$$\mathbf{M}_{t+1} = \beta_1 \mathbf{M}_t + (1 - \beta_1) \nabla_{\text{hor}, t}, \quad (47)$$

$$\mathbf{v}_{t+1} = \beta_2 \mathbf{v}_t + (1 - \beta_2) \nabla_{\text{hor}, t}^2, \quad (48)$$

where $\beta_1 = 0.9$, $\beta_2 = 0.999$, and $\nabla_{\text{hor}, t}^2$ denotes elementwise squaring.

With optional adaptive learning rate (analogous to Adam Kingma and Ba [2015]), the scaled momentum is:

$$\hat{\mathbf{M}}_t = \frac{\mathbf{M}_t / (1 - \beta_1^t)}{\sqrt{\mathbf{v}_t / (1 - \beta_2^t) + \epsilon}}. \quad (49)$$

Without adaptive scaling (the default), we simply use $\hat{\mathbf{M}}_t = \mathbf{M}_t$.

J.2.3 Step 3: Skew-Symmetric Direction

The Cayley retraction requires a skew-symmetric direction matrix:

$$\mathbf{W} = \hat{\mathbf{M}}_t \mathbf{U}^\top - \mathbf{U} \hat{\mathbf{M}}_t^\top \in \mathbb{R}^{n \times n}, \quad \mathbf{W} = -\mathbf{W}^\top. \quad (50)$$

This \mathbf{W} defines a curve on the Stiefel manifold through the current point \mathbf{U} .

J.2.4 Step 4: Iterative Cayley Retraction

The Cayley retraction maps the tangent vector back to the manifold without an explicit matrix inverse:

$$\mathbf{Y}_0 = \mathbf{U} + \alpha \hat{\mathbf{M}}_t, \quad (51)$$

$$\mathbf{Y}_{i+1} = \mathbf{U} + \frac{\alpha}{2} \mathbf{W}(\mathbf{U} + \mathbf{Y}_i), \quad i = 0, \dots, s-1. \quad (52)$$

After s iterations (typically $s = 2$), we update $\mathbf{U} \leftarrow \mathbf{Y}_s$.

J.2.5 Step 5: QR Retraction (Post-Step Correction)

For robustness under DDP gradient synchronization and mixed-precision training, we also apply a QR retraction after each optimizer step:

$$\mathbf{Q}, \mathbf{R} = \text{QR}(\mathbf{U}), \quad (53)$$

$$\mathbf{U} \leftarrow \mathbf{Q} \cdot \text{diag}(\text{sign}(\text{diag}(\mathbf{R}))). \quad (54)$$

The sign correction ensures a unique representative on the Stiefel manifold (the Q -factor from QR is unique up to column sign flips).

The complete Riemannian optimization step is given in Algorithm 9.

Algorithm 9 Cayley ADAM Riemannian Optimization Step

Require: Current basis $\mathbf{U} \in \text{St}(n, p)$, Euclidean gradient $\nabla_{\mathbf{U}} \mathcal{L}$

Require: Momentum state $\mathbf{M}, \mathbf{v}, t$; hyperparameters $\alpha, \beta_1, \beta_2, \epsilon$

Ensure: Updated $\mathbf{U} \in \text{St}(n, p)$

```

1:  $t \leftarrow t + 1$ 
2: ▷ Step 1: Horizontal projection
3:  $\nabla_{\text{hor}} \leftarrow \nabla_{\mathbf{U}} \mathcal{L} - \mathbf{U}(\mathbf{U}^\top \nabla_{\mathbf{U}} \mathcal{L})$ 
4: ▷ Step 2: Momentum update
5:  $\mathbf{M} \leftarrow \beta_1 \mathbf{M} + (1 - \beta_1) \nabla_{\text{hor}}$ 
6:  $\mathbf{v} \leftarrow \beta_2 \mathbf{v} + (1 - \beta_2) \nabla_{\text{hor}}^2$  ▷ Optional adaptive LR
7: if adaptive LR then
8:    $\hat{\mathbf{M}} \leftarrow \frac{\mathbf{M}/(1-\beta_1^t)}{\sqrt{\mathbf{v}/(1-\beta_2^t)+\epsilon}}$ 
9: else
10:   $\hat{\mathbf{M}} \leftarrow \mathbf{M}$ 
11: end if
12: ▷ Step 3: Skew-symmetric direction
13:  $\mathbf{W} \leftarrow \hat{\mathbf{M}}\mathbf{U}^\top - \mathbf{U}\hat{\mathbf{M}}^\top$ 
14: ▷ Step 4: Iterative Cayley retraction
15:  $\mathbf{Y} \leftarrow \mathbf{U} + \alpha \hat{\mathbf{M}}$ 
16: for  $i = 1, \dots, s$  do
17:    $\mathbf{Y} \leftarrow \mathbf{U} + \frac{\alpha}{2} \mathbf{W}(\mathbf{U} + \mathbf{Y})$ 
18: end for
19:  $\mathbf{U} \leftarrow \mathbf{Y}$ 
20: ▷ Step 5: QR retraction (optional, for DDP compatibility)
21:  $\mathbf{Q}, \mathbf{R} \leftarrow \text{QR}(\mathbf{U})$ 
22:  $\mathbf{U} \leftarrow \mathbf{Q} \cdot \text{diag}(\text{sign}(\text{diag}(\mathbf{R})))$ 

```

J.3 DDP/DeepSpeed Integration

The Grassmannian optimization is implemented as a **post-step optimizer wrapper** (`GrassmannianOptimizer` that:

1. Automatically discovers all `GrassmannianProjection` modules in the model (handling DDP/DeepSpeed wrapper unwrapping).
2. After each standard optimizer step (`optimizer.step()`), applies QR retraction to project \mathbf{U} back onto $\text{St}(n, p)$.
3. Maintains its own state dict for momentum (\mathbf{M}), second moment (\mathbf{v}), and time step (t), supporting full checkpoint save/load.
4. All tensor operations use in-place ops and avoid CPU-GPU synchronization (the time step t is kept as a GPU tensor to avoid `.item()` calls that trigger sync).

J.4 Geometric Interpretation

The Grassmannian projector $\mathbf{H}_{\text{res}} = \mathbf{U}\mathbf{U}^\top$ filters the n -dimensional residual stream through a learned p -dimensional subspace. Geometrically:

- Components of \mathbf{x} *within* the subspace $\text{col}(\mathbf{U})$ are preserved.
- Components *orthogonal* to the subspace are projected to zero.
- The sublayer output is added back, potentially reintroducing orthogonal components.

This provides an implicit form of **information bottleneck** in the residual stream, where the model learns which p directions carry the most useful information across layers.